

the duration of the embedded phase of star formation

0 Son Kim,¹ \star Mélanie Chevance,¹ J. M. Diederik Kruijssen,¹
 1 Meas Schruba,² Karin Sandstrom,³ Ashley T. Barnes,⁴ Frank Bigiel,⁴
 Guillermo A. Blanc,^{5,6} Yixian Cao,⁷ Daniel A. Dale,⁸ Christopher M. Faesi,⁹
 Simon C. O. Glover,¹⁰ Kathryn Grasha,¹¹ Brent Groves,¹² Cinthya Herrera,¹³
 Ralf S. Klessen,^{10,14} Kathryn Kreckel,¹ Janice C. Lee,¹⁵ Adam K. Leroy,⁶
 Frédéric Pety,^{16,17} Miguel Querejeta,¹⁸ Eva Schinnerer,¹⁹ Jiayi Sun,¹⁶
 Antonio Usero,¹⁸ Jacob L. Ward,¹ Thomas G. Williams,¹⁹

1 1 See the end of the paper

2 Accepted XX, Received XX; in original form 2020 November 40

3

4 \star

5 \square

6 1 2 3 4 5 6 7 8 9 10 11 12 13 14 15 16 17 18 19 20 21 22 23 24 25 26 27 28 29 30 31 32 33 34 35 36 37 38 39 40 41 42 43 44 45 46 47 48 49 50 51 52 53 54 55 56 57 58 59 60 61 62 63 64 65 66 67 68 69 70 71 72 73 74 75 76 77 78 79 80 81 82 83 84 85 86 87 88 89 90 91 92 93 94 95 96 97 98 99 100 101 102 103 104 105 106 107 108 109 110 111 112 113 114 115 116 117 118 119 120 121 122 123 124 125 126 127 128 129 130 131 132 133 134 135 136 137 138 139 140 141 142 143 144 145 146 147 148 149 150 151 152 153 154 155 156 157 158 159 160 161 162 163 164 165 166 167 168 169 170 171 172 173 174 175 176 177 178 179 180 181 182 183 184 185 186 187 188 189 190 191 192 193 194 195 196 197 198 199 200 201 202 203 204 205 206 207 208 209 210 211 212 213 214 215 216 217 218 219 220 221 222 223 224 225 226 227 228 229 230 231 232 233 234 235 236 237 238 239 240 241 242 243 244 245 246 247 248 249 250 251 252 253 254 255 256 257 258 259 260 261 262 263 264 265 266 267 268 269 270 271 272 273 274 275 276 277 278 279 280 281 282 283 284 285 286 287 288 289 290 291 292 293 294 295 296 297 298 299 300 301 302 303 304 305 306 307 308 309 310 311 312 313 314 315 316 317 318 319 320 321 322 323 324 325 326 327 328 329 330 331 332 333 334 335 336 337 338 339 340 341 342 343 344 345 346 347 348 349 350 351 352 353 354 355 356 357 358 359 360 361 362 363 364 365 366 367 368 369 370 371 372 373 374 375 376 377 378 379 380 381 382 383 384 385 386 387 388 389 390 391 392 393 394 395 396 397 398 399 400 401 402 403 404 405 406 407 408 409 410 411 412 413 414 415 416 417 418 419 420 421 422 423 424 425 426 427 428 429 430 431 432 433 434 435 436 437 438 439 440 441 442 443 444 445 446 447 448 449 450 451 452 453 454 455 456 457 458 459 460 461 462 463 464 465 466 467 468 469 470 471 472 473 474 475 476 477 478 479 480 481 482 483 484 485 486 487 488 489 490 491 492 493 494 495 496 497 498 499 500 501 502 503 504 505 506 507 508 509 510 511 512 513 514 515 516 517 518 519 520 521 522 523 524 525 526 527 528 529 530 531 532 533 534 535 536 537 538 539 540 541 542 543 544 545 546 547 548 549 550 551 552 553 554 555 556 557 558 559 560 561 562 563 564 565 566 567 568 569 570 571 572 573 574 575 576 577 578 579 580 581 582 583 584 585 586 587 588 589 590 591 592 593 594 595 596 597 598 599 600 601 602 603 604 605 606 607 608 609 610 611 612 613 614 615 616 617 618 619 620 621 622 623 624 625 626 627 628 629 630 631 632 633 634 635 636 637 638 639 640 641 642 643 644 645 646 647 648 649 650 651 652 653 654 655 656 657 658 659 660 661 662 663 664 665 666 667 668 669 670 671 672 673 674 675 676 677 678 679 680 681 682 683 684 685 686 687 688 689 690 691 692 693 694 695 696 697 698 699 700 701 702 703 704 705 706 707 708 709 710 711 712 713 714 715 716 717 718 719 720 721 722 723 724 725 726 727 728 729 730 731 732 733 734 735 736 737 738 739 740 741 742 743 744 745 746 747 748 749 750 751 752 753 754 755 756 757 758 759 760 761 762 763 764 765 766 767 768 769 770 771 772 773 774 775 776 777 778 779 780 781 782 783 784 785 786 787 788 789 790 791 792 793 794 795 796 797 798 799 800 801 802 803 804 805 806 807 808 809 810 811 812 813 814 815 816 817 818 819 820 821 822 823 824 825 826 827 828 829 830 831 832 833 834 835 836 837 838 839 840 841 842 843 844 845 846 847 848 849 850 851 852 853 854 855 856 857 858 859 860 861 862 863 864 865 866 867 868 869 870 871 872 873 874 875 876 877 878 879 880 881 882 883 884 885 886 887 888 889 890 891 892 893 894 895 896 897 898 899 900 901 902 903 904 905 906 907 908 909 910 911 912 913 914 915 916 917 918 919 920 921 922 923 924 925 926 927 928 929 930 931 932 933 934 935 936 937 938 939 940 941 942 943 944 945 946 947 948 949 950 951 952 953 954 955 956 957 958 959 960 961 962 963 964 965 966 967 968 969 970 971 972 973 974 975 976 977 978 979 980 981 982 983 984 985 986 987 988 989 990 991 992 993 994 995 996 997 998 999 1000 1001 1002 1003 1004 1005 1006 1007 1008 1009 1010 1011 1012 1013 1014 1015 1016 1017 1018 1019 1020 1021 1022 1023 1024 1025 1026 1027 1028 1029 1030 1031 1032 1033 1034 1035 1036 1037 1038 1039 1040 1041 1042 1043 1044 1045 1046 1047 1048 1049 1050 1051 1052 1053 1054 1055 1056 1057 1058 1059 1060 1061 1062 1063 1064 1065 1066 1067 1068 1069 1070 1071 1072 1073 1074 1075 1076 1077 1078 1079 1080 1081 1082 1083 1084 1085 1086 1087 1088 1089 1090 1091 1092 1093 1094 1095 1096 1097 1098 1099 1100 1101 1102 1103 1104 1105 1106 1107 1108 1109 1110 1111 1112 1113 1114 1115 1116 1117 1118 1119 1120 1121 1122 1123 1124 1125 1126 1127 1128 1129 1130 1131 1132 1133 1134 1135 1136 1137 1138 1139 1140 1141 1142 1143 1144 1145 1146 1147 1148 1149 1150 1151 1152 1153 1154 1155 1156 1157 1158 1159 1160 1161 1162 1163 1164 1165 1166 1167 1168 1169 1170 1171 1172 1173 1174 1175 1176 1177 1178 1179 1180 1181 1182 1183 1184 1185 1186 1187 1188 1189 1190 1191 1192 1193 1194 1195 1196 1197 1198 1199 1200 1201 1202 1203 1204 1205 1206 1207 1208 1209 1210 1211 1212 1213 1214 1215 1216 1217 1218 1219 1220 1221 1222 1223 1224 1225 1226 1227 1228 1229 1230 1231 1232 1233 1234 1235 1236 1237 1238 1239 1240 1241 1242 1243 1244 1245 1246 1247 1248 1249 1250 1251 1252 1253 1254 1255 1256 1257 1258 1259 1260 1261 1262 1263 1264 1265 1266 1267 1



0 properties, across the small galaxy sample for which these measurements are possible. We discuss the robustness of our results by comparing them with the literature in Section 5. Last, we present our conclusions in Section 6.

2 OBSERVATIONAL DATA

1 We apply our analysis to six nearby galaxies: IC 342, the LMC, M33, M51, and NGC 300. The size of our sample is mostly limited by the angular resolution of the *Spitzer* MIPS observations at $24\mu\text{m}$ ($\sim 6.4''$, Rieke et al. 2004; corresponding to $2 - 110$ pc for the galaxies in our sample, including M51 for which we use a map at higher angular resolution, see Section 2.1) and the fact that we need to resolve at least the separation length between star-forming regions undergoing independent evolutionary lifecycles ($100 - 200$ pc) to apply our analysis (see Sections 5.1.1 and Kruiswijk et al. 2018). Here, we provide a summary of the observational methods used to trace the molecular gas (emission from low-J CO transitions), embedded massive stars ($24\mu\text{m}$ emission), and exposed young stellar regions (H α emission). Composite three-color images of the CO, $24\mu\text{m}$, and H α maps are presented in Figure 1, whereas the individual CO and $24\mu\text{m}$ maps are shown in Appendix A. The physical and observational properties of the galaxies in our sample are listed in Table 1.

3 Descriptions of multi-wavelength data sets

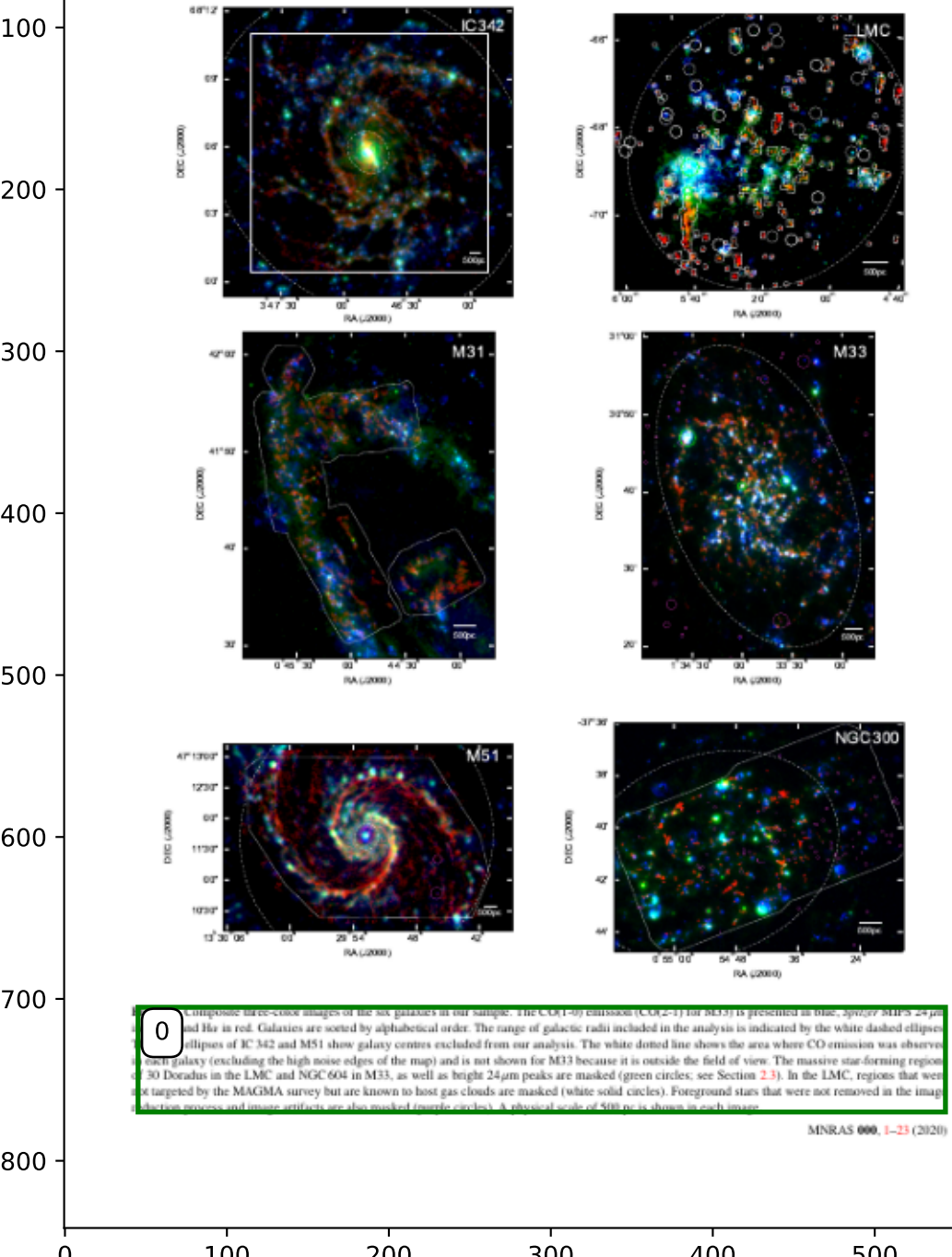
4 The CO data cube is from the ^{12}CO ($J=1-0$) survey of the LMC, with a beam size of $3.6''$, a spectral resolution of 5 km s^{-1} , and a sensitivity of 135 mK per 5 km s^{-1} velocity channel. Integrating over 10 km s^{-1} , this translates to a 5σ point source sensitivity of $5\sigma(M_{\text{H}_2}) \approx 6.1 \times 10^7\text{ M}_\odot$ when the CO($1-0$)-to-H α conversion factor (α_{CO}) listed in Table 1 is assumed. In order to trace molecular gas in IC 342, covering up to 7.7 kpc in galactic radius. The final data cube has a circular beam size of $3.6''$, a spectral resolution of 5 km s^{-1} , and a sensitivity of 135 mK per 5 km s^{-1} velocity channel. Integrating over 10 km s^{-1} , this translates to a 5σ point source sensitivity of $5\sigma(M_{\text{H}_2}) \approx 6.1 \times 10^7\text{ M}_\odot$ when the CO($1-0$)-to-H α conversion factor (α_{CO}) listed in Table 1 is assumed. In order to trace embedded star formation, we retrieve *Spitzer* MIPS $24\mu\text{m}$ image from the Local Volume Legacy (LVL) Survey (Dale et al. 2009). In addition to the procedure described in Dale et al. (2009), we mask foreground stars with a G-band magnitude ≤ 22 mag using the Gaia DR2 catalog (Gaia Collaboration et al. 2018), as well as background galaxies via visual inspection of extended and non-circular sources. We then subtract background emission by fitting a plane determined at $2 - 2.5R_\star$ from the galactic centre where R_\star is the optical radius of the galaxy, obtained from the Lyon Extragalactic Database (Patton et al. 2003a,b; Fardal et al. 2014). H α emission has been observed with the Imager on the Mayall 4-m telescope. We utilise calibrate narrow-band H α and R-band images kindly provided by Kimberl Herrmann (private communication). We post-process these images as described in Schruba et al. (2021a). In brief, we subtract continuum emission from the H α image, mask Milky Way stars using the Gaia DR2 catalog, subtract a sky background by fitting a 1st order polynomial plane at galactic radii > 10 kpc, and correct for Galactic extinction adopting $A(\text{H}\alpha) = 1.3$ mag which is derived from $E(B-V) = 0.494$ mag (Schlafly & Finkbeiner 2011) and is

7 used here, we do not attempt to correct for the internal extinction so that it traces exposed star-forming regions. The resulting H α map has an angular resolution of $0.85''$. Due to limited coverage of the CO survey and blending of bright sources at the galaxy centre, we restrict our analysis to regions where CO observation have been made within galactic radii $1.0 - 7.7$ kpc, as shown in Figure 1.

8 We adopt a distance of 8.0 kpc (Vazquez et al. 2017), an inclination of 22.0° , and a position angle of 168.6° (Meidt et al. 1998). The adopted metallicity at the centre of the LMC is $12 + \log(\text{O/H})_0 = 8.35 \pm 0.03$, with a radial gradient of $0.0105 \pm 0.0105\text{ dex kpc}^{-1}$, as measured by Toribio San Cipriani et al. (2017) using a direct measurement of electron temperature (T_e) from spectra of H α regions (direct T_e -based method). We employ the CO($1-0$) data presented in the third data release of the Magellanic Mopra Assessment (MAGMA; Wong et al. 2011, 2017) to trace molecular gas. MAGMA is a CO mapping survey of the LMC and SMC using the Mopra 22-m Telescope at the Australia Telescope National Facility. For the LMC, the observations were carried out as a follow-up study of the NANTEN survey (Fukui et al. 2008) by targeting a subset of previously identified molecular clouds (~ 160 out of ~ 272 clouds), with an improved resolution in order to resolve the GMCs (~ 11 pc). In Figure 1, white dotted lines show the coverage of the MAGMA survey and solid white circles indicate regions where molecular gas has been detected by the NANTEN survey, but not further targeted with the MAGMA survey. We exclude these white circled regions, where we know GMCs exist, from our analysis¹. However, we still include other regions not observed by the MAGMA survey, which might have diffuse and faint CO emission. We note that the inclusion of these sight lines, not covered by the MAGMA survey, should have a negligible impact on our results because diffuse and faint emission is eventually removed in our analysis through a filtering process (see Section 3). Moreover, the MAGMA survey covers most ($\sim 80\%$) of the total CO emission from the LMC observed by the NANTEN survey (Wong et al. 2011). The observed CO emission from the MAGMA survey also shows good agreement with the molecular gas map produced using dust continuum emission modelling (Jameson et al. 2016), indicating that we cover most of the emission from GMCs. The resulting angular resolution of the MAGMA CO data is $45''$, and the sensitivity is 0.3 K per 5.26 km s^{-1} velocity channel. Integrating over 10 km s^{-1} , this translates to a 5σ point source sensitivity of $5\sigma(M_{\text{H}_2}) \approx 2.2 \times 10^7\text{ M}_\odot$ (assuming the α_{CO} from Table 2). The *Spitzer* MIPS $24\mu\text{m}$ image is from the SAGE project (Meixner et al. 2006), covering $7^\circ \times 7^\circ$ of the galaxy. The continuum-subtracted H α map is from the Southern H-Alpha Sky

10 Survey in the discussion of each galaxy. We do not adopt the same reddening ($E(B-V)$) or the extinction law when correcting for extinction. This is to follow what has been done previously for each galaxy, in our first application of the statistical method using CO and H α emission only (Kruiswijk et al. 2019; Chevance et al. 2020c; Hygate 2020; Ward et al. 2020a). Nevertheless, similarly to the CO($1-0$)-to-H α and SFR conversion factor (see Section 3.2), we note that our choice of correction factor does not affect our measurements of timescales and region separation length, but only the derived total SFR and the integrated star formation efficiency.

¹ Using the cloud catalogue from the NANTEN survey (Fukui et al. 2008) Ward et al. (2020a) have modelled the CO emission from the GMCs that were not observed by MAGMA and have shown that excluding these regions from our analysis has a negligible effect on the measurements.



Physical and observational properties of our galaxy sample									
0	Stellar mass ^a	Metallicity ^{b,c}	Distance	Inclination	Position angle	CO observations	CO resolution	24 μm resolution	Spatial resolution ^d
	[log ₁₀ M _⊙]	[Z/Z _⊙]	[Mpc]	[deg]	[deg]		["]	["]	[pc]
IC 342	10.2 ± 0.1	0.90 ± 0.20	3.45	31.0	42.0	NOEMA + IRAM 30-m	3.6	6.4	107
LMC	9.3 ± 0.1	0.48 ± 0.03	0.05	22.0	168.0	ATNF	45	6.4	11
M31 (NGC 224)	11.0 ± 0.1	0.76 ± 0.20	0.78	77.7	37.7	CARMA	5.5	6.4	24
M33 (NGC 598)	9.4 ± 0.1	0.50 ± 0.06	0.84	55.0	201.1	IRAM 30-m	12	6.4	49
MS1 (NGC 5194)	10.7 ± 0.1	1.37 ± 0.20	8.6	21.0	173.0	PAIBI	1.1	2.4	100
NGC 300	9.3 ± 0.1	0.48 ± 0.06	2.0	42.0	111.0	+ IRAM 30-m ALMA	2.1	6.4	62

^a Taken from [Sakurai et al. \(2007\)](#) for the LMC and [Stock et al. \(2007\)](#) for M31, while others are from [Gratier et al. \(2010\)](#).
^b Minimum weighted metallicity over the considered field of view.
^c Calculated using $Z/Z_{\odot} = (O/H)/(O/H)_{\odot}$, with the solar oxygen abundance $12 + \log(O/H)_{\odot} = 8.69$ ([Asplund et al. 2009](#)).
^d Current spatial resolution of the CO and 24 μm maps.

2 Atlas (SHASSA; [Gutierrez et al. 2001](#)) and has a resolution of 12''. We correct for Galactic extinction using $A(H\alpha) = 0.16$ mag, derived from $E(B-V) = 0.06$ mag ([Staveley-Smith et al. 2003](#)) and an extinction curve with $R_V = 3.1$ ([Cardelli et al. 1989](#)). For the analysis here, we include emission from 0–3 kpc in galactic radius, where the outer boundary is indicated in Figure 1.

3 $\mathrm{H}\alpha$ map at a distance of 9.30 Mpc ([Gratier et al. 2010](#)) has an inclination of 37.7°, and a position angle of 77.7° ([Corradi et al. 2010](#)). The adopted metallicity at the galactic centre is $12 + \log(O/H)_{\odot} = 8.8 \pm 0.1$, with a radial gradient of $-0.022 \pm 0.014 \text{ dex kpc}^{-1}$, as measured by [Zarits & Bresolin \(2012\)](#) using the strong-line calibration from [Pilyugin \(2001\)](#). To trace molecular gas, we use CO(1–0) data first appeared in [Calde-Primo & Schruba \(2016\)](#), with full details presented in [Schruba et al. 2021b](#). This data is obtained by combining CARMA interferometry data and IRAM 30-m data, the latter from [Nieten et al. 2006](#). The CARMA observations cover 87 kpc² of M31's star-forming disc at galactic radii of 6–13 kpc. They have an angular resolution of 1.5'', a spectral resolution of 2.5 km s⁻¹, and a sensitivity of 175 mK per 2.5 km s⁻¹ velocity channel. Integrating over 10 km s⁻¹, this translates to a 5σ point source sensitivity of $5\sigma(M_{\mathrm{H}_2}) = 7.3 \times 10^7 M_{\odot}$ (assuming the α_{CO} from Table 2). We utilise the velocity masked moment-zero map, which is designed to be flux-complete (see [Schruba et al. 2021b](#) for details). We employ the *Spitzer* MIPS 24 μm map presented in [Gordon et al. 2006](#). This map is already background-subtracted, and we refer the reader to the original paper for more information on the data reduction procedure. The Hα emission map is discussed in [Schruba et al. \(2018\)](#) and has been created from calibrated narrow-band Hα and R-band images from the Local Group Galaxies Survey (LGGS; [Massey et al. 2006](#)). The observations were carried out by the MOSAIC Imager on the Mayall 4-m telescope. The calibrated data were post-processed as described in [Schruba et al. \(2021b\)](#), which include Hα continuum subtraction, masking of Milky Way stars using the Gaia DR2 catalog ([Gaia Collaboration et al. 2018](#)), sky background subtraction by fitting a plane at galactic radii > 20 kpc, and a correction for the contamination by [N II] by assuming that both [N II] lines contribute 35% of the total Hα emission following [Azimlu et al. \(2011\)](#). The Galactic extinction is corrected by adopting a factor $A(H\alpha) = 0.14$ mag, which is derived from $E(B-V) = 0.05$ mag ([Schlafly & Finkbeiner 2011](#)) and an extinction curve with $R_V = 3.1$ ([Cardelli et al. 1989](#)). The resulting Hα

is an angular resolution of 1.5''. We perform our analysis in a field of view spanned by the CO observations.

4 $\mathrm{H}\alpha$ map at a distance of 1.84 Mpc ([Gratier et al. 2010](#)) has an inclination of 55.0°, and a position angle of 201.1° ([Koch et al. 2018](#)). The adopted metallicity at the galactic centre is $12 + \log(O/H)_{\odot} = 8.48 \pm 0.04$, with a radial gradient of $-0.042 \pm 0.010 \text{ dex kpc}^{-1}$, as measured by [Bresolin \(2011\)](#) using a direct T_c -based method. We use the $^{12}\mathrm{CO}(J=2-1)$ transition (denoted as CO(2–1) in the following) data presented in [Gratier et al. \(2010\)](#) and [Druard et al. \(2014\)](#) to trace molecular gas. The observations were carried out using the HETerodyne Receiver Array (HERA; [Schuster et al. 2004](#)) on the IRAM 30-m telescope covering the galaxy out to radii of 7 kpc. The resulting angular resolution is 12'' and the average noise level is 20 mK per 2.6 km s⁻¹ velocity channel. Integrating over 10 km s⁻¹, this noise level translates to a 5σ point source sensitivity of $5\sigma(M_{\mathrm{H}_2}) = 6.2 \times 10^7 M_{\odot}$ (assuming the α_{CO} from Table 2). We retrieve *Spitzer* MIPS 24 μm images from the Local Volume Legacy (LVL) Survey ([Dale et al. 2009](#)). We then apply the same post-processing procedures as described above for IC 342. The narrow-band Hα data is from [Greenawalt \(1998\)](#). The observations were carried out using the Burrell-Schmidt 0.6-m telescope at the Kitt Peak National Observatory (KPNO). Details information about the image reduction process can be found in [Hoopes & Walterbos \(2000\)](#). The Galactic extinction is corrected by using $A(H\alpha) = 0.1$ mag, obtained from $E(B-V) = 0.0413$ mag ([Schlegel et al. 1998](#)) and an extinction curve with $R_V = 3.1$ ([Fitzpatrick & Massa 2007](#)). The resolution of the Hα emission map is 2.0''. We restrict our analysis to galactocentric radii ≤ 5 kpc, as outlined in Figure 1.

5 $\mathrm{H}\alpha$ map at a distance of 11.0 Mpc ([Gratier et al. 2010](#)) has an inclination of 21.0°, and a position angle of 173.0° ([Colomb et al. 2014](#)). The adopted metallicity at the galactic centre is $12 + \log(O/H)_{\odot} = 8.88 \pm 0.053$, with a radial gradient of $-0.0223 \pm 0.0037 \text{ dex kpc}^{-1}$, as measured by [Pilyugin et al. \(2014\)](#) using the strong-line “counterpart” method ([Pilyugin et al. 2012](#)). We use the CO(1–0) data of the inner 10×6 kpc² of the M51 presented in [Pety et al. \(2013\)](#) as part of the PAIBI Arcsecond Whirlpool Survey (PAWS; [Schinnerer et al. 2013](#)). The surveyed region is visible in Figure 1. The PAIBI observations were carried out using A, B, C and D configurations. The IRAM 30-m telescope was used to recover emission at low spatial frequencies. The final data have an angular resolution of 1.1'' and a sensitivity of 0.39 K per 5 km s⁻¹ velocity channel. Integrating over 10 km s⁻¹, this noise level trans-

6 $\mathrm{H}\alpha$ map at a distance of 9.30 Mpc ([Gratier et al. 2010](#)) has an inclination of 21.0°, and a position angle of 173.0° ([Colomb et al. 2014](#)). The adopted metallicity at the galactic centre is $12 + \log(O/H)_{\odot} = 8.88 \pm 0.053$, with a radial gradient of $-0.0223 \pm 0.0037 \text{ dex kpc}^{-1}$, as measured by [Pilyugin et al. \(2014\)](#) using the strong-line “counterpart” method ([Pilyugin et al. 2012](#)). We use the CO(1–0) data of the inner 10×6 kpc² of the M51 presented in [Pety et al. \(2013\)](#) as part of the PAIBI Arcsecond Whirlpool Survey (PAWS; [Schinnerer et al. 2013](#)). The surveyed region is visible in Figure 1. The PAIBI observations were carried out using A, B, C and D configurations. The IRAM 30-m telescope was used to recover emission at low spatial frequencies. The final data have an angular resolution of 1.1'' and a sensitivity of 0.39 K per 5 km s⁻¹ velocity channel. Integrating over 10 km s⁻¹, this noise level trans-

lates to a 5 σ point source sensitivity of $5\sigma(M_{\mathrm{H}_2}) \approx 8.9 \times 10^4 M_{\odot}$, using the α_{CO} from Table 2). The integrated intensity map was created by applying a mask to the data cube as described in Petty et al. (2013). Due to the limited resolution of *Spitzer* MIPS 24 μm imaging (6. $4''$; Rieke et al. 2004), we can in principle only apply our method to galaxies closer than ~ 5 Mpc. However, using the higher resolution (2. $4''$) 24 μm map created by Dumas et al. (2011), we are able to expand the application of our method to M51, located at 8.6 Mpc. This map was created by applying the HiRes deconvolution algorithm (Buckas et al. 2005) to the 5th *Spitzer* Infrared Nearby Galaxies Survey (SINGS; Kennicutt et al. 2003) data delivery (see Dumas et al. 2011 for more details). However, we note that the artifacts introduced by the deconvolution algorithm could potentially bias our analysis, especially for timescale-related quantities, by modifying the distribution of the 24 μm flux around bright peaks, limiting the interpretation of our results for this galaxy. The H α emission map is also from SINGS (Kennicutt et al. 2003). The observations were carried out using the KPNO 2.1-m telescope with the CFIM imager. The map is corrected for Galactic extinction adopting a correction factor $A(\text{H}\alpha) = 0.08$ mag, obtained from $E(B-V) = 0.03$ mag (Schlafly & Finkbeiner 2011) and an extinction curve with $R_V = 3.1$ (Fitzpatrick 1999). We also correct for the contamination by [N II] lines by scaling the map by a factor of 0.7. The resolution of the H α emission map is 1.83''. Because we lack CO observations of the outer galaxy and sources at the galaxy centre are affected by crowding and contamination from active galactic nucleus, we restrict our analysis to the field of view of the CO observations, and within galactic radii of 0.51–5.35 kpc, as indicated in Figure 1.

IC 342, M33, and NGC 300 have an inclination of 42.0°, and a position angle of 111.0° (West et al. 2011). We adopt a metallicity of $12 + \log(\text{O/H})_0 = 8.46 \pm 0.05$ at the galactic centre and a radial gradient of -0.056 ± 0.015 dex kpc $^{-1}$, as measured by Toribio San Cipriano et al. (2016) using a direct T_{ν} -based method. We employ ALMA observations of the CO(1–0) transition, from ALMA programmes 2013.1.00351.S and 2015.1.00258.S (PI A. Schruba), to be presented in A. Schruba et al. (in preparation) and first used in Kruissjen et al. (2019). The observations were performed using the 12-m main array, as well as the 7-m array and total power antennas of the ALMA Compact Array, covering galactic radii out to 4.8 kpc. The resulting data have angular resolution of 2.1'' (~ 20 pc) and sensitivity of 0.1 K per 2 km s $^{-1}$ channel. Integrating over 10 km s $^{-1}$, this noise level translates to a 5 σ point source sensitivity of $5\sigma(M_{\mathrm{H}_2}) \approx 4.3 \times 10^3 M_{\odot}$, assuming the α_{CO} from Table 2. We retrieve *Spitzer* MIPS 24 μm image from the Local Volume Legacy (LVL) Survey (Dale et al. 2009) and apply the same post-processing procedures as described above for IC 342. We use the H α image presented in Faes et al. (2014). This map is created from narrow-band H α data and nearby continuum available in the ESO data archive, and we use here the version kindly shared by Chris Faesi (private communication). The observations were carried out with the Wide Field Imager (WFI) in the MPG/ESO 2.2-m telescope at La Silla observatory. Correction for Galactic extinction is applied using $A(\text{H}\alpha) = 0.027$ mag, obtained from $E(B-V) = 0.01$ mag (Schlafly & Finkbeiner 2011) and an extinction curve with $R_V = 3.1$ (Fitzpatrick 1999). We remove contamination of [N II] lines by assuming an intensity ratio $(\text{N II})/I(\text{H}\alpha) = 0.2$. The resolution of the map is 1.35''. In our analysis, we consider emission from the field of view of the CO observations, and within 0–3 kpc in galactic radius (beyond which the molecular gas surface density drops precipitously), and the outer boundary is visible in Figure 1.

REGULARIZATION OF MAPS TO COMMON PIXEL GRID

To apply our analysis, the gas and SFR tracer maps for each galaxy need to share the same pixel grid. Therefore, for each map we regrid the map with a smaller pixel size to match the pixel grid of the map with larger pixel size. When the map that is being regressed has a better spatial resolution than the reference map, we first convolve the map with a Gaussian kernel to the resolution of the reference map before regressing to avoid introducing artifacts⁷.

CONSTRUCTION OF MASKS

The small-scale variation of the gas-to-SFR flux ratios is seen in the evolutionary timeline of the molecular clouds (see Fig. 3). By definition, our measurements are flux-weighted averages (see Kruissjen et al. 2018), which implies that very bright peaks dominating a significant fraction of the total flux can bias our results. Therefore, we mask star-forming regions in some galaxies that are clear outliers in the luminosity function of SFR tracer peaks. Specifically, we first sort the peak fluxes (identified using CLUMPFIND; see Section 3) in descending order. We then look for a gap in the distribution by calculating the ratio of the flux between the n^{th} brightest and the next brightest peak in line, starting from the brightest peak. A gap is defined to exist when the n^{th} peak is more than twice as bright as the $(n+1)^{\text{th}}$ peak. Whenever a gap is found, we mask all the peaks that are brighter than the $(n+1)^{\text{th}}$ brightest peak. As a result, we mask three star-forming regions each in the LMC and in M33 before applying our analysis (green circles in Figure 1). These regions include 30 Doradus in the LMC and NGC 604 in M33, which alone contribute more than 30% of the 24 μm emission of each galaxy. Note that we would be masking the same peaks unless we go down to a brightness difference of 50% (rather than 100%) when defining a gap in the luminosity function. In this case, we would be masking one to four more peaks each in IC 342, M33, and NGC 300. The impact of masking such bright regions on the resulting derived parameters is generally small when averaging over the entire galaxy, but becomes significant if a smaller fraction of the galaxy is considered (see Ward et al. 2020a for the effect of 30 Doradus on the LMC and Chevance et al. 2020c for the effect of the “headlight cloud” on the spiral galaxy NGC 628, also see Herrera et al. 2020). We also check for bright regions that satisfy this condition in the CO emission maps, but found none. Finally, we also mask artifacts in the maps (purple circles in Figure 1).

THOD

Using a statistical method (constrained to the filamentary case) to constrain the evolutionary timeline of GMCs. This timeline can be decomposed into the cloud lifetime (which continues until dispersal of molecular clouds), and the star formation tracer lifetime. The characteristic separation length between star-forming regions undergoing independent evolution is also constrained in our analysis. Here, we provide a summary of the methodology and the main input parameters. We refer the reader to Kruissjen & Longmore (2014) for a detailed explanation of the method, to Kruissjen et al.

⁷ Convolving the 24 μm map, we have also tested using a more extensive kernel (Antano et al. 2011) and found that the use of a Gaussian kernel has negligible impact on our results.

0 In the presentation and validation of the Heintz code, we provide the full list of input parameters, and to Chevance et al. (2020c) for a general application of the method to nine nearby star-forming galaxies. The accuracy of the method has been demonstrated in Kruissjen et al. (2018) using simulated galaxies, and has since been confirmed through extensive observational and numerical testing (Kruissjen et al. 2019; Haydon et al. 2020a; Ward et al. 2020b).

Description of the analysis method

1 The analysis is composed of numerous tracers and star-forming regions. The fundamental concept of our method is that such regions are independently undergoing their evolution, from molecular clouds to the formation of stars. These evolutionary phases are observed using gas (e.g. CO) and SFR tracers (e.g. H α or 24 μm). We define the duration of each phase based on the visibility timescale of the tracers used. The timescale during which a gas emission tracer and an SFR tracer co-exist corresponds to the duration of massive star formation plus the time it takes to disrupt its natal molecular gas by stellar feedback (i.e. the feedback timescale, t_{fb}). In the following, the cloud lifetime will be denoted as t_{CO} , the star formation tracer lifetime as $t_{\text{H}\alpha}$ or $t_{24\mu\text{m}}$, and the feedback timescale as $t_{\text{fb},\text{H}\alpha}$ or $t_{\text{fb},24\mu\text{m}}$, depending on the SFR tracer used.

2 Using the initial phase of cloud evolution, a given snapshot is only visible in the molecular gas tracer. As the cloud disperses and starts forming stars, the region becomes visible both in the gas and SFR tracers. Eventually, the remaining molecular gas is dispersed by stellar feedback and the region is only visible in the SFR tracers. Locally, the gas-to-SFR flux ratio therefore decreases with time during the evolution of a cloud. Observationally, when focusing on a non-star-forming GMC, a higher gas-to-SFR flux ratio is measured compared to the large-scale (~ 1 kpc) average gas-to-SFR flux ratio. By contrast, when focusing on a young star-forming region, where most of the molecular gas has been dispersed, a lower gas-to-SFR flux ratio is measured. The deviations of the small-scale gas-to-SFR flux ratio compared to the large-scale average, as a function of spatial scale, can be directly related to the duration of the different phases of the GMC lifecycle (Kruissjen &

3 4, 5, 6). In the following, we focus mainly on the gas-to-SFR flux ratio in emission maps. We then convolve both maps into a range of spatial resolutions spanning from $I_{\text{ap,min}}$ to $I_{\text{ap,max}}$ (see Table 2). The maximum aperture size ($I_{\text{ap,max}}$) is set to a value that is close to the size of the major axis of the deprojected beam of the coarsest resolution between the two maps, whereas the maximum aperture size ($I_{\text{ap,min}}$) covers most of the galaxy. For each convolved map, apertures with the size of the corresponding resolution are placed in the identified gas and SFR tracer peaks. We then measure the gas and SFR tracer flux enclosed in these apertures to obtain the gas-to-SFR flux ratios as a function of aperture size. By fitting an analytical model describing the gas-to-SFR flux ratio as a function of the aperture size and the underlying evolutionary timescales, we obtain a direct measurement of these timescales. This can be understood with an idealised example. For a tracer that is longer lived, more peaks are typically identified, covering a larger fraction of the galaxy when small apertures are centred on them, compared to the shorter-lived tracer. The measured flux ratio is therefore closer to the galactic average value for a longer-lived tracer than a shorter-lived one.

6 The analytical model derived by Kruissjen et al. (2018)

7 measured flux ratios in order to constrain the relative durations of the different phases of the molecular cloud and star-forming lifecycle, as well as the typical separation length between independent regions (λ). The absolute duration of the different phases is then obtained by scaling the relative duration of timescales with a reference timescale (t_{ref}). In our previous analyses using CO and H α observations (Kruissjen et al. 2019; Chevance et al. 2020c; Hygate 2020; Ward et al. 2020a), we used the duration of the isolated H α emitting phase ($t_{\text{H}\alpha} = t_{\text{H}\alpha} - t_{\text{fb},\text{H}\alpha}$), calibrated by Haydon et al. (2020a) using the stellar population synthesis model SLUG2 (da Silva et al. 2012, 2014; Krumholz et al. 2015), as the reference timescale. Here, in order to obtain absolute values when applying our analysis to CO and 24 μm maps, we first apply the method to CO and H α observations. This is to obtain the cloud lifetime (t_{CO}) and its upward and downward uncertainties ($t_{\text{CO},\text{upper}}$ and $t_{\text{CO},\text{lower}}$, see Table 3), which are adopted as the reference timescale (t_{ref}) and its uncertainties ($t_{\text{ref},\text{upper}}$ and $t_{\text{ref},\text{lower}}$) in the analysis with CO and 24 μm observations. The fitted model is thus described by three independent and non-degenerate quantities ($t_{24\mu\text{m}}, t_{\text{H}\alpha}$, and λ). The best-fitting values are then obtained by minimising the reduced χ^2 over these three quantities. The uncertainties of each parameter are propagated consistently throughout the analysis.

8 Using a large-scale component that is not associated with the compact peaks. This large-scale emission potentially includes diffuse emission originating from sources related to the recent massive star formation, such as low mass molecular clouds, low luminosity H α regions, and ionizing photons that have escaped from H α regions (e.g. Wood et al. 2010; F. Belfiore et al. in preparation). It may also originate from other mechanisms not related to recent massive star formation, for example, diffuse molecular gas, infrared emission powered by stars of intermediate age, and diffuse ionized gas created by shocks (Martin 1997; Leroy et al. 2012). We remove such diffuse emission in both gas and SFR tracer emission maps iteratively, using the method presented in Hygate et al. (2019), which makes the derived timescales sensitive to only the massive/luminous molecular clouds and young stellar populations. This method filters emission on spatial scales larger than n_1 times the typical distance between regions λ (as measured from the Heintz code) using a Gaussian high-pass filter in Fourier space. For each galaxy, we adopt the smallest possible value for n_1 , while ensuring the flux loss from the compact emission to be less than 10% (also following Chevance et al. 2020c; Hygate 2020, see Table 2). We do not adopt a fixed filtering scale because we want to maximise the removal of diffuse emission, while minimising the impact of the filtering on the compact regions. The influence of n_1 on the derived timescales is fully described in Hygate et al. (2019) and Hygate (2020). In summary, the choice of n_1 does not significantly change the best-fitting model parameters, as long as the adopted n_1 is smaller than 30 and the flux loss from the compact emission is less than 10%. After the diffuse emission is filtered out, a noise mask with a threshold at twice the standard deviation noise level of the emission map is applied. We repeat this process until the convergence condition is reached, which is when the change of the measured value of λ is less than 5% over three consecutive iterations.

Input parameters

9, 10 Otherwise noted here, we adopt the same parameters as for analyses using H α as an SFR tracer (see Appendix B for M31, Ward et al. 2020a for the LMC, Hygate 2020 for

Input parameters of the analysis using 24 μm as SFR tracers for each galaxy. Other parameters not mentioned here are the same as in our previous analysis using H _α as an SFR tracer.							
Galaxy	IC342	LMC	M31	M33	M51	NGC 300	Description
$l_{\text{ap,max}} [\text{pc}]$	116	25	52	65	90	60	Minimum aperture size to convolve the input maps to
$l_{\text{ap,max}} [\text{pc}]$	3000	2000	3000	2500	3000	2500	Maximum aperture size to convolve the input maps to
N_{ap}	15	15	15	15	15	15	Number of aperture sizes used to create array of logarithmically-spaced aperture size in the range ($l_{\text{ap,min}}, l_{\text{ap,max}}$)
$N_{\text{pix,peak}}$	20	10	20	20	10	100	Minimum number of pixels for a valid peak
$\Delta \log_{10} \mathcal{F}_{\text{CO}}$	2.0	2.5	1.3	2.2	2.5	2.0	Logarithmic range below flux maximum covered by flux contour levels for molecular gas peak identification
$\Delta \log_{10} \mathcal{F}_{\text{CO}}$	0.05	0.15	0.02	0.10	0.05	0.10	Logarithmic interval between flux contour levels for molecular gas peak identification
$\Delta \log_{10} \mathcal{F}_{\text{24μm}}$	3.8	2.8	2.3	3.0	4.0	2.0	Logarithmic range below flux maximum covered by flux contour levels for SFR tracer peak identification
$\Delta \log_{10} \mathcal{F}_{\text{24μm}}$	0.05	0.05	0.05	0.10	0.05	0.10	Logarithmic interval between flux contour levels for SFR tracer peak identification
$t_{\text{ref}} [\text{Myr}]$	20.0	11.1	14.0	14.5	30.5	10.8	Reference timescale spanned by molecular gas tracer
$\sigma t_{\text{ref,down}} [\text{Myr}]$	2.3	1.7	1.9	1.5	4.8	1.7	Downwards uncertainty on reference timescale
$\sigma t_{\text{ref,up}} [\text{Myr}]$	2.0	1.6	2.1	1.6	9.2	2.1	Upwards uncertainty on reference timescale
$\text{SFR} [\text{M}_\odot \text{yr}^{-1}]$	0.97	0.12	0.041	0.18	1.63	0.063	Total SFR in the analysed area
$\sigma(\text{SFR}) [\text{M}_\odot \text{yr}^{-1}]$	0.19	0.03	0.008	0.04	0.32	0.013	Uncertainty of the total SFR
$\log_{10} \alpha_{\text{CO}}$	0.65	0.83	0.69	0.81	0.59	0.82	Logarithm of CO(1–0)-to-H ₂ conversion factor
$\sigma_{\text{rel}}(\alpha_{\text{CO}})$	0.5	0.5	0.5	0.5	0.5	0.5	Relative uncertainty of α_{CO}
μ_L	13	7	10	10	16	8	Characteristic width for the Gaussian filter used to remove diffuse emission in Fourier space

1 The parameters not mentioned here include distance, inclination, position angle (see Table 1), as well as parameters related to the fitting process and error propagation, for which default values are adopted as listed in Kruisjens et al. (2018). We use Clempner & Williams (1994) to identify gas and SFR tracer peaks in each map. This algorithm finds peaks by drawing closed contours for a set of flux levels, within a given flux range ($\Delta \log_{10} \mathcal{F}$) below the maximum flux level, with an interval of $\Delta \log_{10} \mathcal{F}$ between flux levels. The adopted values for our sample are summarised in Table 2. Moreover, to avoid identifying point sources that are likely to be foreground stars that were not masked during the image reduction process or externally illuminated starless dust clumps (see Section 3.3), we only accept peaks that contain more than $N_{\text{pixels,peak}}$ pixels. The area of $N_{\text{pixels,peak}}$ pixels equals 0.2–3.5 times the coarsest beam size. We note that our choices of $\Delta \log_{10} \mathcal{F}$, $\log_{10} \mathcal{F}$, $N_{\text{pixels,peak}}$, N_{ap} , and N_{pix} do not affect our measurements significantly as long as peaks that are obviously visible in the emission maps have been identified (Kruisjens et al. 2018). As explained above, ζ_{CO} and its uncertainties determined from our analysis with CO and H_α are used to define the reference timescales (t_{ref}). However, since we additionally mask some of the bright star-forming regions for the reasons explained in Section 2.3, we re-run the same analysis using H_α as an SFR tracer with updated masks. Our measurements using H_α as an SFR tracer are listed in Table 3, and are in very good agreement with (or identical to) the previously published results for the analysis with CO and 24 μm. t_{ref} (= t_{CO}) includes the feedback phase. The CO(1–0)-to-H₂ conversion factor (α_{CO} ; including the contribution from heavy elements) is adopted from Bolatto et al. (2013), expressed as

$$\alpha_{\text{CO}} = [2.9 M_\odot (\text{K km s}^{-1} \text{ pc}^2)^{-1}] \times \exp\left(\frac{0.4 Z_\odot}{Z}\right). \quad (1)$$

2 We adopt the metallicity-dependent part, but not the surface dependence from Bolatto et al. (2013). For simplicity, we adopt a constant α_{CO} value for each galaxy and a conservative uncertainty of 20%.

3 In addition, for M33, which is the only galaxy with CO(1–0) data, we adopt a fixed ratio of CO(2–1)/CO(1–0) = 0.3 (Calzetti et al. 2010). Finally, we derive the total SFR for the analysed area by combining 24 μm and H_α emission maps and using the conversion factor from Calzetti et al. (2007), expressed as

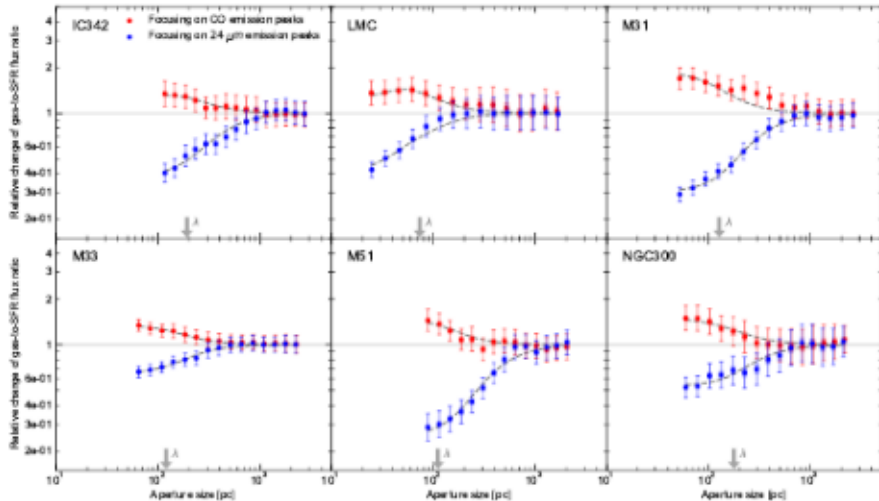
$$4 \text{SFR} [\text{M}_\odot \text{yr}^{-1}] = 5.3 \times 10^{-4} [L(\text{H}\alpha) + 0.031 L(24 \mu\text{m})]. \quad (2)$$

5 The luminosities have units of erg s⁻¹ and L(24 μm) is expressed as $vL(v)$. We assume a typical uncertainty of 20% for the SFR. These conversion factors are only used to derive additional physical quantities such as the molecular gas surface density and the integrated star formation efficiency. We note that the exact values of these conversion factors, unless they vary spatially do not affect our measurements of primary quantities, which are the durations of the successive phases of cloud evolution and star formation, nor do they affect the region separation length between independent regions.

RESULTS

molecular cloud lifecycle

6 present our results from the application of our method to maps of CO and 24 μm emission presented in Section 2, a comparison of the molecular gas and the SFR for six nearby galaxies. Figure 2 shows the gas-to-SFR flux ratios measured around gas and SFR tracer peaks, as a function of aperture size, together with our best-fitting model for each galaxy. Going towards smaller aperture sizes (from ~1 kpc to ~50 pc), the measured flux ratios for both tracers increasingly deviate from the galactic average, illustrating the spatial de-correlation between the gas and SFR tracer emission peaks. Table 3 summarises the constrained best-fitting values from applying our analysis to the H_α and CO maps, as well as the 24 μm and CO maps. The first experiment allows us to measure t_{CO} , which is then used as the reference timescale for the second experiment (see Section 3). Table 3 also lists other physical



0 The relative change of the gas-to-SFR (CO vs 24 μm) mass ratio compared to the galactic average as a function of the size of apertures placed on CO (blue) and 24 μm (red) emission peaks. The error bars indicate 1 σ uncertainty on each individual data point whereas the shaded area is an effective 1 σ uncertainty taking into account the covariance between data points. The galactic average is shown as the solid horizontal line and the dashed line indicates the best-fitting model. The constrained region separation length (λ) is indicated in each panel with the downward arrow and other constrained best-fitting parameters ($t_{\text{H}_2, \text{CO}}$ and $t_{\text{H}_2, 24\mu\text{m}}$) are listed in Table 3.

1 Physical quantities constrained using the method described in Section 3, describing the evolution of molecular clouds to exposed or embedded stellar systems traced by H α and 24 μm , respectively. Following the notation throughout this paper, t_{CO} is the cloud lifetime, $t_{\text{H}_2, \text{H}\alpha}$ and $t_{\text{H}_2, 24\mu\text{m}}$ are the duration of partially exposed and embedded star-forming phase, respectively, and v_{fb} and ϵ_{sf} are the duration of H α and 24 μm emitting phase, respectively. The region separation length (λ) measured with different SFR tracers, feedback velocity (v_{fb}), and star-formation efficiency (ϵ_{sf}) are also listed.

Galaxy	CO vs H α				CO vs 24 μm				v_{fb} [km s $^{-1}$]	ϵ_{sf} (per cent)
	t_{CO} [Myr]	$t_{\text{H}_2, \text{H}\alpha}$ [Myr]	t_{H_2} [Myr]	λ [pc]	$t_{\text{H}_2, 24\mu\text{m}}$ [Myr]	t_{H_2} [Myr]	λ [pc]			
IC 342	$20.0^{+2.0}_{-2.3}$	$2.2^{+0.4}_{-0.5}$	$6.4^{+0.5}_{-0.6}$	120^{+10}_{-10}	$5.2^{+1.5}_{-2.3}$	$7.9^{+1.8}_{-2.2}$	190^{+29}_{-62}	$14.3^{+4.0}_{-1.8}$	$1.9^{+1.8}_{-0.8}$	
LMC	$11.1^{+1.6}_{-1.7}$	$1.3^{+0.2}_{-0.2}$	$5.8^{+0.6}_{-0.6}$	71^{+13}_{-10}	$5.0^{+1.6}_{-2.0}$	$13.6^{+3.7}_{-4.8}$	73^{+38}_{-26}	$10.0^{+2.1}_{-1.7}$	$6.8^{+4.9}_{-3.0}$	
M31	$14.0^{+2.1}_{-1.9}$	$1.1^{+0.3}_{-0.2}$	$5.5^{+0.6}_{-0.5}$	181^{+28}_{-19}	$2.4^{+1.4}_{-0.8}$	$4.2^{+1.5}_{-0.7}$	128^{+97}_{-23}	$29.5^{+6.8}_{-5.3}$	$0.7^{+0.2}_{-0.2}$	
M33	$14.5^{+1.6}_{-1.8}$	$3.3^{+0.6}_{-0.5}$	$7.9^{+0.7}_{-0.7}$	155^{+30}_{-28}	$6.8^{+2.1}_{-2.0}$	$11.9^{+2.9}_{-2.1}$	119^{+90}_{-35}	$10.3^{+1.5}_{-1.3}$	$3.5^{+2.5}_{-1.5}$	
M51	$30.7^{+8.7}_{-4.9}$	$4.7^{+2.0}_{-1.1}$	$8.9^{+2.0}_{-1.2}$	140^{+25}_{-17}	$< 4.0^{\circ}$	$3.6^{+1.2}_{-0.9}$	$< 136^{\circ}$	$7.9^{+2.0}_{-2.1}$	$3.3^{+2.9}_{-1.4}$	
NGC 300	$10.8^{+2.2}_{-1.8}$	$1.5^{+0.2}_{-0.2}$	$6.1^{+0.2}_{-0.2}$	104^{+22}_{-18}	$4.9^{+1.2}_{-1.9}$	$7.9^{+1.8}_{-2.1}$	178^{+128}_{-75}	$9.4^{+0.8}_{-0.7}$	$3.3^{+2.6}_{-1.4}$	

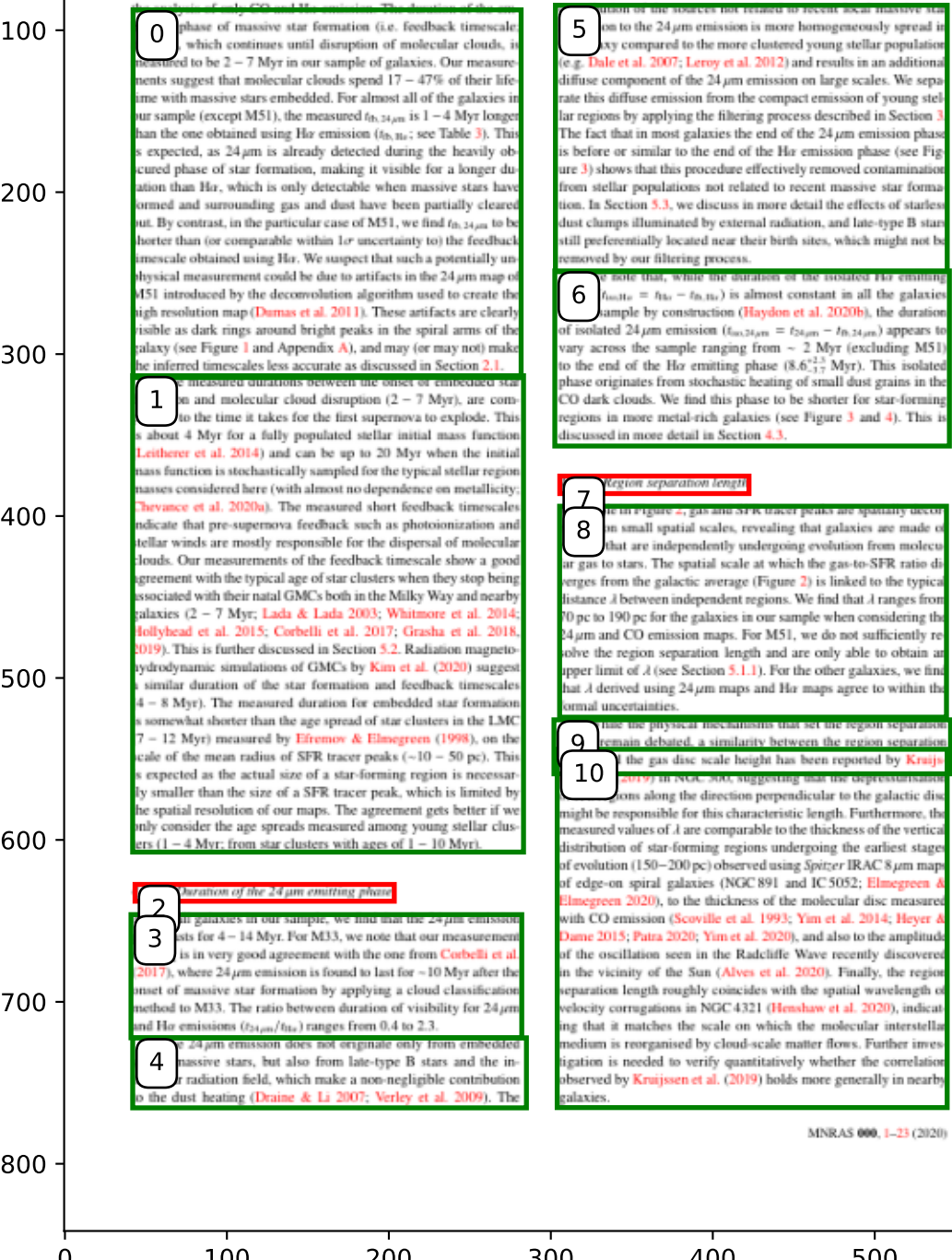
Note: An upper limit can be derived for $t_{\text{H}_2, 24\mu\text{m}}$ if not satisfying Eq. (1) and (10) in Section 3.1.1.

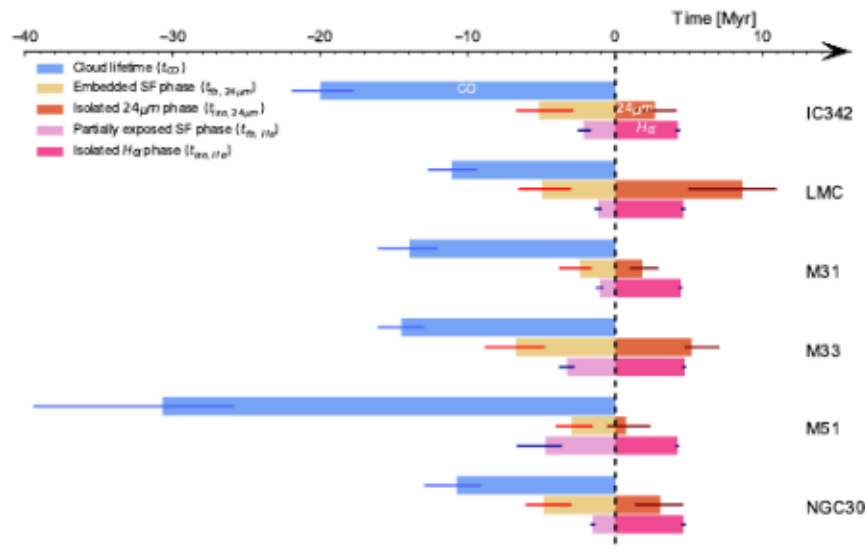
3 Parameters which can be derived from our measurements, such as the feedback outflow velocity (v_{fb} ; see Section 4.1.5) and the integrated molecular cloud-scale star formation efficiency (ϵ_{sf} ; see Section 4.1.4). In Figure 3, we show an illustration of the evolutionary timelines of molecular clouds and star-forming regions in our galaxy sample. GMCs initially emit only in CO, then in 24 μm after the onset

4 of star formation and finally in H α when the star-forming regions become (partially) exposed.

Feedback timescale

5 of 24 μm emission enables us to take the heavily obscured star formation into account, which cannot be done with





0 Timeline describing the evolution from molecular clouds to the embedded star-forming phase and then finally to exposed young stellar regions. The time during which CO is visible ($\approx t_{CO}$) is indicated in orange, the time during which $24\mu m$ and H α are visible without CO are shown respectively in dark and light purple. The timescales for the feedback phase, during which both CO and SFR tracer emissions are observed co-spatially are shown in light blue (for $24\mu m$) and light purple (for H α). The corresponding 1 σ error bars are also indicated. We note that for M51 the feedback timescale constrained using $24\mu m$ ($t_{CO, 24\mu m}$) could have been biased by deconvolution artifacts (see Section 4.1.1).

Star formation efficiency

1 surface density (Σ_{SFR}) corresponds to the mass of newly stars inferred for a given SFR tracer, divided by that SFR emission timescale. Similarly, the rate of molecular gas formation can be expressed as Σ_{gas}/t_{CO} , where Σ_{gas} is the surface density of molecular gas and the t_{CO} is the timescale over which molecular gas assembles and forms stars. By dividing these two rates, the time-averaged star formation efficiency per star-forming event (ϵ_{sf}) can be computed as:

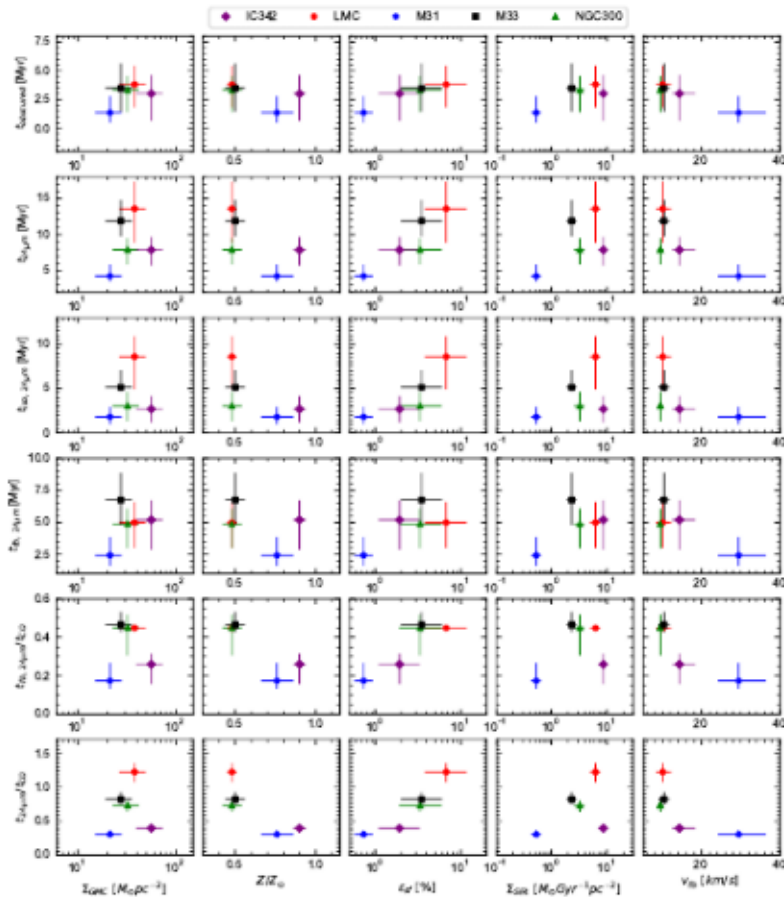
$$\epsilon_{sf} = \frac{t_{CO}\Sigma_{SFR}}{\Sigma_{gas}}. \quad (3)$$

2 calculating Σ_{gas} , we only consider the compact CO emission after filtering of diffuse emission (see Section 3), which is also consistent with the flux we use to determine t_{CO} . By doing this, we selectively include the CO emission that participates in the massive star formation process while excluding emission that is likely to originate from diffuse molecular gas and small clouds. The filtering process removes 10% to 50% of the CO emission from the unfiltered maps. However, Σ_{gas} is calculated using the total SFR obtained by combining H α and $24\mu m$ emission to account for the effect of internal extinction (see Section 2). We note that our assumption implies that we attribute all of the diffuse emission in SFR tracer maps to recent massive star formation (e.g., leakage of

photons from H α regions). This ignores the fact that diffuse emission may also originate from mechanisms that are not recent massive star formation, such as diffuse ionized gas created by shocks and evolved post-asymptotic giant branch stars, as well as infrared emission powered by older stellar populations which are known to have a relatively minor contribution to the dust heating (Nesvorný et al. 2020). Under these conditions, we measure a low star formation efficiency per star-forming event in our sample of galaxies with $\epsilon_{sf} = 0.7 - 6.8\%$. This is consistent with previous measurements in these galaxies using H α as a tracer of recent star formation and other wavelengths such as GALEX FUV and WISE 22 μm (Leroy et al. 2012, 2019) to estimate the global SFR (Chevance et al. 2020c; Hygate 2020; Ward et al. 2020a). We note that for NGC 300, we find ϵ_{sf} to be slightly higher (but compatible within 1 σ uncertainty) than that measured in Kruissel et al. (2019). The difference is because Kruissel et al. (2019) only considered H α emission when calculating the global SFR.

3 also compare our measurements for ϵ_{sf} to the fraction converted into stars per gravitational free-fall time, which is defined as $\epsilon_{sf} = t_{ff}\Sigma_{SFR}/\Sigma_{gas}$ and measured by Leroy et al. 2017, Ulfhake et al. 2018, and Schruba et al. (2019) for most of the galaxies in our sample. We find that our measurements for the LMC, M31, M33, and NGC 300 are somewhat (< 4.0%) higher than the star formation efficiency per free-fall time (ϵ_{sf}) measured by Schruba





0 In the top four rows, our measurements of the duration of the nearly obscured phase ($t_{24,\text{sf}} = t_{24,24\mu\text{m}} - t_{24,34\mu\text{m}}$), the 24-μm emitting phase ($t_{24,\text{em}}$), the 24-μm emitting phase ($t_{24,24\mu\text{m}}$), and the feedback phase ($t_{24,24\mu\text{m}} - t_{24,34\mu\text{m}}$) are shown as a function of galactic (or cloud-scale) properties, mass-weighted mean molecular gas surface density of GMCs (Σ_{GMC}) measured in Scherbin et al. (2019) and Scherbina et al. (2021a), metallicity (Z/Z_{\odot}), star formation efficiency (ϵ_{σ}), SFR surface density (Σ_{SFR}) and the feedback velocity (v_B). The bottom two rows show the ratios of the feedback timescale and the 24-μm emitting phase to the cloud lifetime ($t_{24,\text{sf}}/\text{t}_{\text{cloud}}$ and $t_{24,\text{sf}}/\text{t}_{\text{em}}$), as a function of the same galactic properties.

5.1.1.1. CONCLUSION

5.1.1.2. Robustness of the result

5.1.1.3. Satisfaction of guidelines in Kruissel et al. (2018)

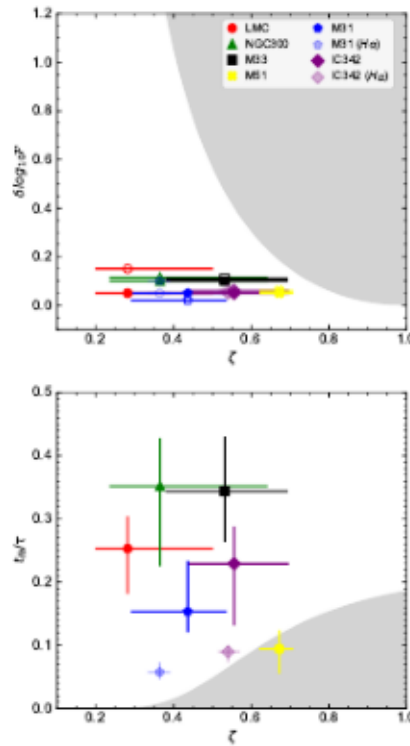
We find that our analysis satisfies the requirements listed in Kruissel et al. (2018). Satisfaction of these criteria implies that the constrained parameters $t_{24,\text{sf}}$, $t_{24,\text{em}}$, and λ are

obtained with an accuracy of at least 30%. For the analysis using Σ_{GMC} as an SFR tracer, we only check the accuracy for IC 342 and the LMC, because the measurements for other galaxies have already been validated by previous studies (see Kruissel et al. 2019; Bouwens et al. 2020b; Hwang 2020; Ward et al. 2020a).

5.1.1.4. The duration of gas and stellar phases should always differ by at least one order of magnitude. This condition is satisfied by



- 0** $|\log_{10}(t_{\text{CO}})| \leq 0.5$ for 86, 84% and 61, and $|\log_{10}(t_{24\mu\text{m}}/t_{\text{CO}})| \leq 0.5$ for all the galaxies in our sample, where the difference between $t_{24\mu\text{m}}$ and t_{CO} is the largest in M51 while those for other galaxies are $|\log_{10}(t_{24\mu\text{m}}/t_{\text{CO}})| \leq 0.52$.
- 1** For almost all of the galaxies (except IC 342), we measure $M_{\text{gas,rest}}$, which ensures that the region separation length is fully resolved by our observations. For M51, we measure $\lambda = 1.2l_{\text{spars}}$, implying that $t_{24\mu\text{m}}$ can be constrained with sufficient accuracy, but only upper limits can be derived for λ and t_{CO} .
- 2** The number of identified emission peaks is always above 1 in the CO and the 24- μm emission maps, as well as in the maps of IC 342 and M31.
- 3** The measured gas-to-SFR flux ratio focusing on gas (SFR) peaks should never be below (above) the galactic average. This condition may not always be true in the presence of a diffuse emission reservoir. As visible in Figure 2, this criterion is satisfied after we filter out the large-scale diffuse emission in both tracer maps.
- 4** In order to perform accurate measurements, we require the star formation history to not vary more than 0.2 dex during the duration of the whole evolutionary cycle (ranging from ~ 15 to ~ 35 Myr for our sample) when averaged over time intervals of width $t_{24\mu\text{m}}$ or t_{CO} . Using multi-wavelength data of the LMC and synthetic stellar population models, Harris & Zanttilis (2009) studied the star formation history in the LMC and found a roughly constant SFR during the duration of the whole evolutionary cycle. The criterion is also satisfied in M33 and NGC 300 as shown by Kang et al. (2012, 2016) using chemical evolution models to reconstruct the star formation rate history. Using data from the PHAT survey, the recent star formation history of M31 is confirmed to be quiescent without significant variations (Lewis et al. 2015; Williams et al. 2017). By performing spectral energy distribution fitting to the multi-wavelength data of M51, the SFR in M51 is also measured to be roughly constant for the last 100 Myr (Efrasio et al. 2017). The star formation history of IC 342 is not known. However, we do not expect it to experience significant variations in the global star formation rate during the last ~ 30 Myr when averaged over $t_{24\mu\text{m}} = 8$ Myr. In addition, we mask the starburst nucleus of this galaxy, which experienced a major burst of star formation ~ 60 Myr ago (Boker et al. 1999).
- 5** Each independent region should be detectable at given sensitivity in both tracers at some point in their life. In order to check if this condition is satisfied in our sample of galaxies, we first calculate the minimum star-forming region mass expected to form from the detected molecular clouds by multiplying the star formation efficiency obtained in our method (see Table 3) by the 5σ point-source sensitivity limit of the CO map. We then compare this mass to the mass of the stellar population required to provide an ionizing radiation luminosity that matches the 5σ sensitivities of 24- μm and H α maps on the scale of individual star-forming regions (λ). We use the Starburst99 model (Leitherer et al. 1999) to calculate the initial mass of the stellar population assuming stars formed instantaneously 5 Myr ago (similarly to the H α emitting timescale). Since Starburst99 only provides models for the H α luminosity as a function of the age of the stellar population at different metallicities, we use the relation from Kennicutt & Evans (2012, and references therein), $\log \text{SFR} = \log(L_{\text{H}\alpha}) - 41.27 = \log(\psi L_{24\mu\text{m}}) - 42.69$, to obtain a similar estimation of the 24- μm luminosity. We find that the minimum mass of the stellar population obtained from CO maps agrees well with that obtained from 24- μm and H α maps (ranging from $100 M_{\odot}$ to $5000 M_{\odot}$ for the galaxies in our sample), suggesting that the sensitivity of the gas and SFR tracer maps are well-matched.
- 6** The CO and the faintest CO peak is likely to evolve into the same ion. In principle, clouds can disperse dynamically before forming massive stars and then reassemble. In this case, the time spent before GMC dispersal would be added by our method to the measured lifetimes of clouds that do form massive stars. However, Kruissel et al. (2019) and Chevance et al. (2020c) show that this is unlikely to happen because the clouds are found to live only for about one dynamical timescale, not leaving enough time for clouds to disperse and recollapse before forming massive stars.
- 7** The upper limits on our measurements of $t_{24\mu\text{m}}$ and λ for the galaxies in our sample as well as the t_{CO} and λ for IC 342 and M31 with H α as SFR tracer are validated by satisfying the conditions listed above. The only exception is for M51, where we neither have sufficient resolution to accurately constrain the region separation length nor the feedback timescale. Only upper limits can be obtained for these values. In order to determine whether our measurements are reliable for $t_{\text{H}\alpha}$ for all the galaxies in our sample and $t_{\text{H}\alpha}$ for IC 342 and M31, we use four additional criteria listed in Kruissel et al. (2018). To do so, we first introduce the filling factor f_{fill} .
- 8** If gas peaks as $\zeta = 2r/\lambda$, where r is the mean radius of the blending peaks. This parameter characterises how densely the peaks are distributed in a map.
- 9** If peaks are densely distributed and potentially overlapping each other, the density contrast used for peak identification (δ) should be small enough to identify adjacent peaks. We compare in Figure 5 our values for $\delta \log_{10} \mathcal{F}$ with the upper limits prescribed by Kruissel et al. (2018) and show that our choice enables the appropriate detection of neighbouring peaks, even in densely populated environments.
- 10** For an accurate measurement of the feedback timescale by neighboring peaks should be small enough. In the case of overlap of neighbouring peaks due to low resolution or blending can be falsely attributed to a temporal overlap, therefore artificially increasing the duration of the measured feedback timescale. In this case, only an upper limit on the feedback timescale can be determined. In Figure 5, we compare the analytical prescription of Kruissel et al. (2018) with our measurements of $t_{\text{H}\alpha}/r$ and average ζ , where r is the total duration of the whole evolutionary cycle ($\tau = t_{\text{CO}} + t_{24\mu\text{m}} - t_{\text{H}\alpha, 24\mu\text{m}}$). The average ζ is obtained by weighting the filling factors for gas and SFR tracer peaks by their corresponding timescales. We find that this condition is not satisfied for $t_{\text{H}\alpha, 24\mu\text{m}}$ in M51. Only upper limits on this quantity can be determined (see Table 3).
- 11** Condition (v) shows that the conditions (vi)–(viii) are also verified for all galaxies.
- 12** Similarly to condition (v), the SFR should not vary more than 0.2 dex during the entire timeline when averaged over the feedback timescale. This condition is also satisfied using the same reasoning, as stated in (v) above.
- 13** After masking obvious blended regions such as artifacts, visual inspection of the maps does not reveal abundant artifacts.
- 14** We find that our measurements are reliable except for $t_{24\mu\text{m}}$ in M51. These two measurements should formally be considered as upper limits as they do not satisfy condition (ii) and (viii). However, we note that the deconvolution artifact present in the 24- μm map of M51 may (or may not) bias the feedback timescale and therefore the value we obtain as the upper limit should be considered uncertain.



0 Effects of blending on the feedback timescale measurements. The top panel shows the adopted density contrasts ($\delta \log_{10} \ell$) used for peak identification in each $24\mu\text{m}$ (filled symbols) and CO (open symbols) emission maps, as a function of the average filling factor ζ . The transparent markers for IC 342 and M31 indicate the adopted $\delta \log_{10} \ell$ and measured ζ for the analysis with H α as SFR tracer. The shaded area indicates the region of the parameter space where peak identification is affected by blending (Krajniak et al. 2019). Our results are well outside of the shaded area, confirming that $\delta \log_{10} \ell$ is small enough ($\delta \log_{10} \ell < 0.1$) to identify adjacent peaks even in maps with a low filling factor. The bottom panel shows the ratio between the feedback timescale (t_0) and the total duration of the whole evolutionary cycle (t) as a function of the average filling factor. The grey shaded area indicates the region of the parameter space where the contamination by neighbouring peaks affects the measurement of the feedback time. As a result, only an upper limit can be measured for $t_{0,24\mu\text{m}}$ in M31, whereas accurate measurements can be made for all other galaxies.

Effects of spatial resolution and inclination on the measured quantities

2 To test the potential effect of spatial resolution on our measurements, we have degraded the resolution of the CO and $24\mu\text{m}$ emission maps of NGC 300 to the coarsest resolution among our galaxy sample (107 pc, see Table 1) and repeated the analysis described in Section 3. We choose NGC 300 for this test as it does not require bright star-forming regions to be masked like in the LMC and M33, making the application of the method more straightforward. We find that timescales ($t_{0,107} = 8.4^{+3.8}_{-2.3}$ Myr; $t_{0,24\mu\text{m}} = 4.8^{+1.5}_{-2.6}$ Myr) and the mean separation length ($\lambda = 217^{+105}_{-112}$ pc) measured at a different spatial resolution are consistent within 1 σ uncertainties with the results of Table 3, confirming previous resolution tests on simulated galaxies (Krajniak et al. 2018) and on NGC 300 (Krajniak et al. 2019) using H α as a SFR tracer.

3 We have also examined the possible effect of inclination on our measurements by repeating the analysis on CO and $24\mu\text{m}$ emission maps of NGC 300, which have been artificially inclined further to match the highest inclination angle among our galaxy sample (M31; $i = 77.7^\circ$). We find that measured timescales ($t_{0,24\mu\text{m}} = 0.4^{+1.2}_{-2.0}$ Myr; $t_{0,24\mu\text{m}} = 3.9^{+1.0}_{-0.9}$ Myr) and the mean separation length ($\lambda = 192^{+109}_{-110}$ pc) agree within 1 σ uncertainties with those of NGC 300 from Table 3. This is already expected from a similar test performed by Krajniak et al. (2018) using simulated galaxies, where our method has been shown to provide reliable measurements even for a highly inclined galaxy as long as independent star-forming regions are sufficiently resolved ($\lambda \geq 1.5 t_{0,24\mu\text{m}}$; see (ii) in Section 5.1.1).

Comparison with other works

5 The duration of the embedded star-forming phase has been measured in M33 by Corbelli et al. (2017), using IRAM CO data and a multi-wavelength infrared source catalog created by Sharma et al. (2011). In their work, GMCs and star-forming regions are classified into different evolutionary stages based on the presence of CO emission and SFR tracers such as $24\mu\text{m}$ and H α or UV emission. The clouds are defined to be in an inactive stage when no sign of star formation is detected, an embedded star-forming phase when CO emission is observed in association with $24\mu\text{m}$ but without associated H α or FUV emission. The region is defined to be at an exposed star-forming phase when H α or FUV emission becomes visible.

6 Age estimates of the exposed star-forming regions (referred to as C-type in Corbelli et al. 2017) from spectral energy distribution (SED) fitting are available in Sharma et al. (2011), and are obtained using photometric data at various wavelengths simultaneously, such as UV, H α , and $24\mu\text{m}$. The age of the C-type phase corresponds to the time it takes for the cloud to evolve from the end of the heavily obscured phase of star formation (observed with $24\mu\text{m}$ but without H α) to the end of the exposed young stellar region phase (both $24\mu\text{m}$ and H α are observed). This duration therefore corresponds to $t_{24\mu\text{m}} - t_{\text{decad}}$ in our analysis. Corbelli et al. (2017) find that the C-type phase in M33 lasts for 8 Myr (without quoted uncertainty), which is in excellent agreement with our measurement of $8.4^{+3.8}_{-2.3}$ Myr. For the duration of the heavily obscured phase of star formation (CO and $24\mu\text{m}$ emission without H α ; referred to as B-type), Corbelli et al. (2017) find 2.4 Myr, which is similar to the duration we measure, not only for M33 ($3.5^{+1.2}_{-1.9}$ Myr), but for most of the galaxies in our sample ($1.4 - 3.8$ Myr; see Section 4.2). Lastly, as for the duration of the inactive phase (referred to as A-type), we measure $t_{\text{CO}} - t_{0,24\mu\text{m}} = 7.7^{+1.4}_{-1.7}$ Myr, which is

than longer than the measurement of 4 Myr from Corbelli et al. (2017). However, given the uncertainties in age estimates using SED fitting (on the order of 0.1 dex) and the absence of any uncertainties on their estimates, the evolutionary timeline of molecular clouds of M33 from Corbelli et al. (2017) and our analysis are in good agreement.

It has also been measured using wavelengths other than 24 μm for the embedded star formation. Calzetti et al. (2015) have measured ages of young massive star clusters in the dwarf starburst galaxy NGC 5253 by applying SED modeling techniques in UV-optical-near infrared *Hubble Space Telescope* photometry. While the star clusters have ages spanning from 1 to 15 Myr, the age estimate of one very heavily attenuated cluster with a clear near-infrared excess indicates that the duration of the heavily obscured phase of star formation is longer than (or similar to) 1 Myr for this particular star-forming region. Whitmore et al. (2014) used free-free radio continuum emission to detect heavily obscured star-forming regions, and characterised the evolutionary timeline from quiescent molecular clouds to exposed star-forming phase using age estimates from SED fitting of young stellar regions in the overlap region of the merging Antennae galaxies. The duration of the heavily obscured phase (referred to as Stage 2 in Whitmore et al. 2014) and the feedback timescale (including the embedded phase, referred to as Stage 3 in Whitmore et al. 2014) are measured to be 1.1 – 1 Myr and 1 – 3 Myr, somewhat shorter than the duration we measure with 24 μm , which are 1 – 4 Myr and 2 – 7 Myr, respectively. We note that this difference could be because (i) the measurements are for galaxies undergoing a merger, unlike our sample; (ii) a different tracer is used to trace embedded star formation; and (iii) age estimates in highly extinguished regions have considerable uncertainties (Hollyhead et al. 2015).

Conclusively, despite differences in numerous, wavelength axes used when constraining the evolutionary cycle of star-forming regions, our results are in good agreement with the measured timescales for the heavily obscured phase and feedback phase found in previous literature. The key step made in the present paper is to generalise these results to a sample of five galaxies (except M51), analysed homogeneously with a single analysis framework that is agnostic about which entities constitute a GMC or star-forming region.

5 Effects of infrared emission not associated with local massive star formation

4 Infrared emission is widely used as a tracer for embedded star formation as it captures emission of massive stars that has been re-emitted by dust grains (see e.g. Calzetti et al. 2007; Kennicutt & Evans 2012; Vutisalchavakul & Evans 2013). However, one of the known issues with using 24 μm emission to trace recent star formation is that the interstellar radiation field, late-type B stars (age of \sim 100 Myr), and dust clumps heated by external radiation such as nearby star-forming regions also contribute to the emission at this wavelength (Calzetti et al. 2007; Murphy et al. 2011; Kennicutt & Evans 2012; Lesov et al. 2012).

5 A difference in spatial distributions associated with each generating 24 μm emission allows us to separate the emission of recent star formation events from other sources. The 24 μm emission originating from the interstellar radiation field has an extended morphology, because it originates from small dust grains in the diffuse interstellar medium (Draine & Li 2007; Draine et al. 2007; Verley et al. 2009; Robitson et al. 2011; Leroy et al. 2012).

6 The same emission, constituting on average of 35% of the 24 μm emission, is therefore expected to be removed during our filtering process.

7 One other issue are effects of λ -bias estimation because late-type B stars and starless dust clumps might not be filtered out due to the emission from young star-forming regions. To estimate the effect of late-type B stars and externally illuminated dust clump on our measurements, we make use of the far-infrared source catalogue of the LMC provided by Seale et al. (2014). In this catalogue young stellar objects and dust clumps (that may or may not have deeply embedded forming stars) are identified, as well as source not related to recent star formation such as asymptotic giant branch stars, planetary nebulae, and supernova remnants using literature catalogs (Seale et al. 2014 and references therein). In order to test whether the inclusion of 24 μm emission from older stars and dust clumps could bias our results, we mask these sources and repeat our analysis of the LMC. When masking dust clumps, we mask all the probable candidates in Seale et al. (2014) as it is difficult to distinguish whether these clumps harbour deeply embedded stars or are heated by external radiation. We find that the older stars and dust clumps have a negligible effect on our results. In practice, older stars and dust clumps are not usually identified as SFR tracer peak in our analysis due to their low brightness and small size, which does not satisfy the requirement of a minimum number of pixels to be identified as a peak in our method.

8 In conclusion, once the diffuse emission has been filtered, the maps mostly contain emission from young stars. Any potential bias due to the interstellar radiation field, late-type B stars, and dust clumps is negligible and our measurements of $t_{24,\text{ini}}$ provide an accurate characterisation of the duration of (partially) embedded massive stars.

6 CONCLUSION

9 At a characterisation of the evolutionary timeline from molecular clouds to young stellar regions in six nearby galaxies using the statistical method developed by Kruissel et al. (2018) to CO and 24 μm emission maps at cloud-scale (20–100 pc) resolution. With this method, we measure the duration of the 24 μm emission phase ($t_{24,\text{ini}}$), the duration of the feedback phase ($t_{\text{fb},24,\text{ini}}$) during which massive star formation continues embedded in molecular clouds, the duration of the heavily obscured star formation phase with no associated H α emission ($t_{\text{dust,ini}}$), and the average distance between independent star-forming regions evolving from clouds to massive star formation ($\langle d \rangle$). We also derive other physical quantities such as the feedback velocity (v_{fb}) and the integrated star formation efficiency per star formation event (ϵ_{sf}) from our measurements.

10 As our sample of galaxies, we find that molecular clouds are disrupted within 2 – 7 Myr after the onset of embedded star formation (traced by 24 μm emission) by stellar feedback, supporting the fact that GMCs are dispersed within a cloud dynamical timescale, as suggested by Elmegreen (2000) and Hartmann (2001). The measured feedback timescale, which includes the duration of the massive star-forming phase, constitutes 17–47% of the cloud lifetime of 10 – 30 Myr. The feedback timescales are generally shorter than the time it takes for the first supernova to explode (4 – 20 Myr), when stochasticity of the initial mass function is taken into account (Chevance et al. 2020a), suggesting that early feedback mechanisms such as photoionization and stellar winds are

0 have found similar duration of this phase using age estimates of clusters in the Milky Way and some nearby galaxies (Lada & Lada 2003; Whitmore et al. 2014; Corbelli et al. 2017). After the molecular gas is dispersed, the $24\mu\text{m}$ emission decays within 2–9 Myr. Our results further support the conclusion of earlier work that galaxies are composed of independent star-forming regions separated by ~ 100 – 200 pc (Kruissel et al. 2019; Chevance et al. 2020c), which may correspond to the vertical gas disc scale height (see Kruissel et al. 2019). These regions are undergoing an inefficient star-forming process with integrated cloud-scale star formation efficiencies (ϵ_{sf}) of 0.7–6.8%. The measured star formation efficiencies are consistent with previous measurements in these galaxies using other tracers to estimate the global SFR. We obtain feedback velocities (v_{fb}) of 8 – 30 km s^{-1} , which is consistent with the observed expansion velocities of nearby H II regions (e.g. Murray & Rahman 2010; McLeod et al. 2019, 2020; Barnes et al. 2020).

1 or exposed star-forming regions, we also measure the duration of the heavily obscured phase (detected with CO and $24\mu\text{m}$ but without H α emission). Our results show that this period lasts for 3.0 ± 0.9 Myr (with a full range of 1.4 – 3.8 Myr across our sample of galaxies). We do not detect any significant correlation of the duration of this heavily obscured phase with galactic properties. This measured duration is in good agreement with values suggested by previous works using different wavelengths, methods, and galaxies.

2 Furthermore, we study the correlation of our measurements with Galactic (or cloud-scale) properties, such as mass-weighted surface density of GMCs, metallicity, star formation efficiency, SFR surface density, and the feedback velocity. While we do not find statistically significant trends, the durations of the total and isolated $24\mu\text{m}$ emission phases ($t_{24\mu\text{m}}$ and $t_{\text{iso},24\mu\text{m}}$) may weakly decrease with increasing metallicity. We conjecture that this dependence results from winds of massive stars being stronger and more energetic at higher metallicities, which leads to a more effective dispersal of the clouds. No such trends with metallicity are observed for the feedback timescale and the duration of the heavily obscured phase.

3 In order to gain a better understanding of the mechanisms driving the early feedback process, a systematic measurement of the obscured phase in a large number of galaxies in various environments is essential. Due to the limited resolution of *Spitzer* $24\mu\text{m}$ observations ($6.4''$), we have been able to perform this analysis for only six nearby galaxies and accurately constrain the duration of the embedded phase in five of them. In the future, the MIRI imager aboard the *James Webb Space Telescope*, with a field of view of $1' \times 2'$, will reach an angular resolution of $0.7''$. This will enable the application of the same method to galaxies located out to 25 Mpc, covering a much wider range of galaxy properties and morphologies, allowing us to explore how the feedback processes govern the evolution of molecular clouds during the early stages of star formation, as a function of the galactic environment.

ACKNOWLEDGEMENTS

4 We thank an anonymous referee for helpful comments that improved the quality of the manuscript. We thank Alexander Hyatt for thoughtful suggestions and K. Herrmann for kindly sharing the H α map of IC 342. JK, MC, and JMDK gratefully acknowledge funding from the German Research Foundation (DFG)

6 as the DFG Sachbeihilfe (grant number KR4801/2-1). JK, MC, and JMDK gratefully acknowledge funding from the DFG through an Emmy Noether Grant (grant number KR4801/1-1). JMDK gratefully acknowledges funding from the European Research Council (ERC) under the European Union's Horizon 2020 research and innovation programme via the ERC Starting Grant MUSTANG (grant agreement number 714907). JMDK gratefully acknowledges funding from Sonderforschungsbereich SFB 881 (Project-ID 138713538) 'The Milky Way System' (sub-project B2) of the DFG. PB and ATB would like to acknowledge funding from the European Research Council (ERC) under the European Union's Horizon 2020 research and innovation programme (grant agreement No.726384/Empire). SCOG and RSJ acknowledge support from the Deutsche Forschungsgemeinschaft (DFG) via the Collaborative Research Center (SFB 881, Project ID 138713538) "The Milky Way System" (sub-projects A1, B1, B2 and B8) and from the Heidelberg cluster of excellence (EXC 2181 – 390900948) "STRUCTURES: A unifying approach to emergent phenomena in the physical world, mathematics, and complex dat", funded by the German Excellence Strategy. They also thank for funding from the European Research Council in the ERC Synergy Grant "ECOGAL – Understanding our Galactic ecosystem: From the disk of the Milky Way to the formation sites of stars and planets" (project ID 855130). KK gratefully acknowledges funding from the German Research Foundation (DFG) in the form of an Emmy Noether Research Group (grant number KR4598/2-1, PI Kreckel). The work of AKL and JS is partially supported by the National Science Foundation (NSF) under grant Nos. 1615105, 1615109, and 1653300. MQ acknowledges support from the research project PID2019-106027GA-C44 from the Spanish Ministerio de Ciencia e Innovación. ES and TGW acknowledge funding from the European Research Council (ERC) under the European Union's Horizon 2020 research and innovation programme (grant agreement No. 694343). This work was carried out as part of the PHANGS collaboration. This paper makes use of the following ALMA data: ADS/JAO.ALMA #2013.1.00351.S, ADS/JAO.ALMA #2015.1.00258.S. ALMA is a partnership of ESO (representing its member states), NSF (USA) and NINS (Japan), together with NRC (Canada), NSC and ASIAA (Taiwan) and KASI (Republic of Korea), in cooperation with the Republic of Chile. The Joint ALMA Observatory is operated by ESO, AUI/NRAO, and NAOJ. The National Radio Astronomy Observatory is a facility of the National Science Foundation operated under cooperative agreement by Associated Universities, Inc. This work makes use of the PdBI Arcsecond Whirlpool Survey (Pety et al. 2013; Schinnerer et al. 2013). The authors thank IRAM for making the data products of IC 342 (Schubert et al. 2021a), M31 (Schubert et al. 2021b), and M33 CO Large Program (Gratier et al. 2010; Draine et al. 2014) available. IRAM is supported by INSU/CNRS (France), MPG (Germany), and IGN (Spain). We thank the IRAM staff for their assistance with the observations.

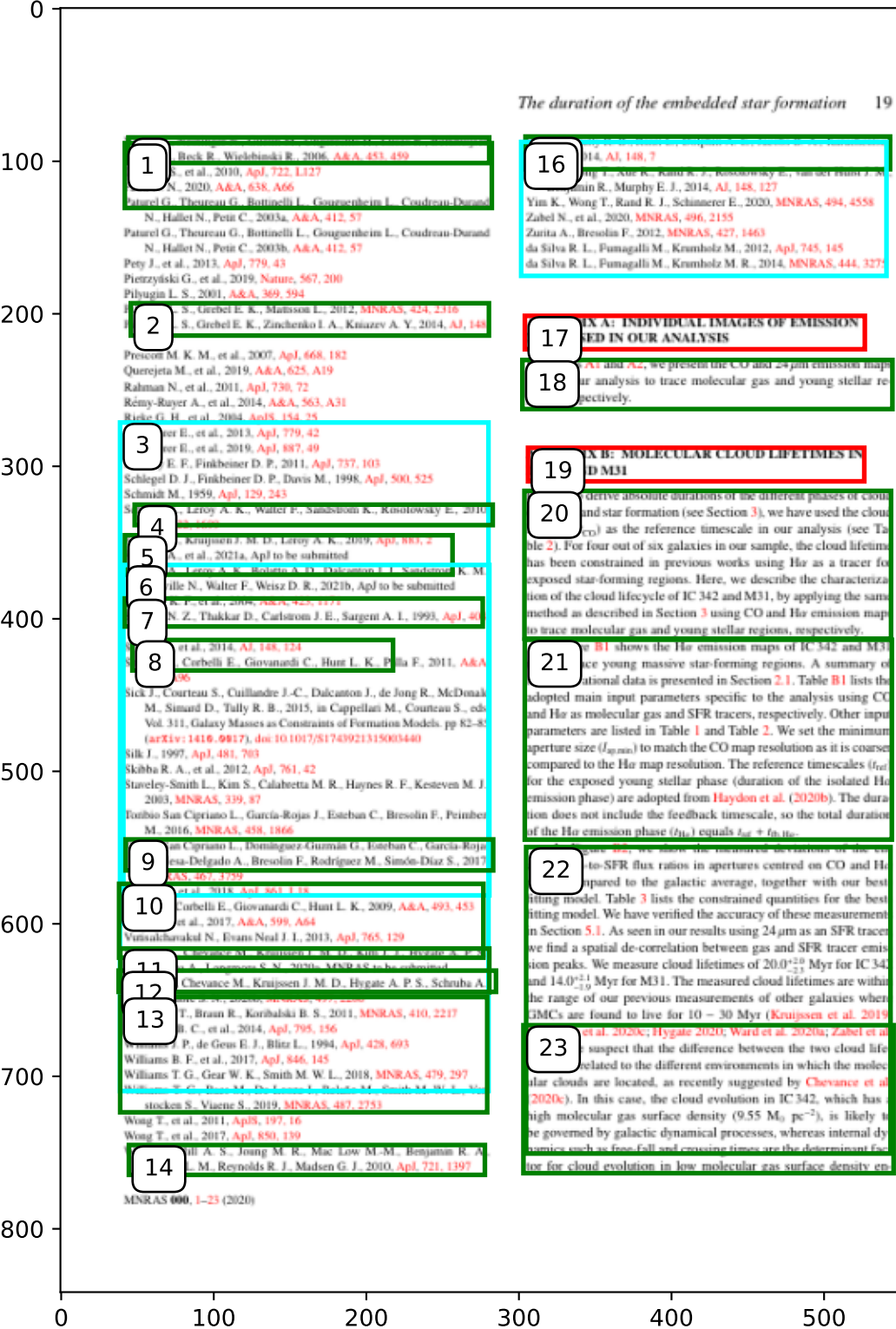
AVAILABILITY

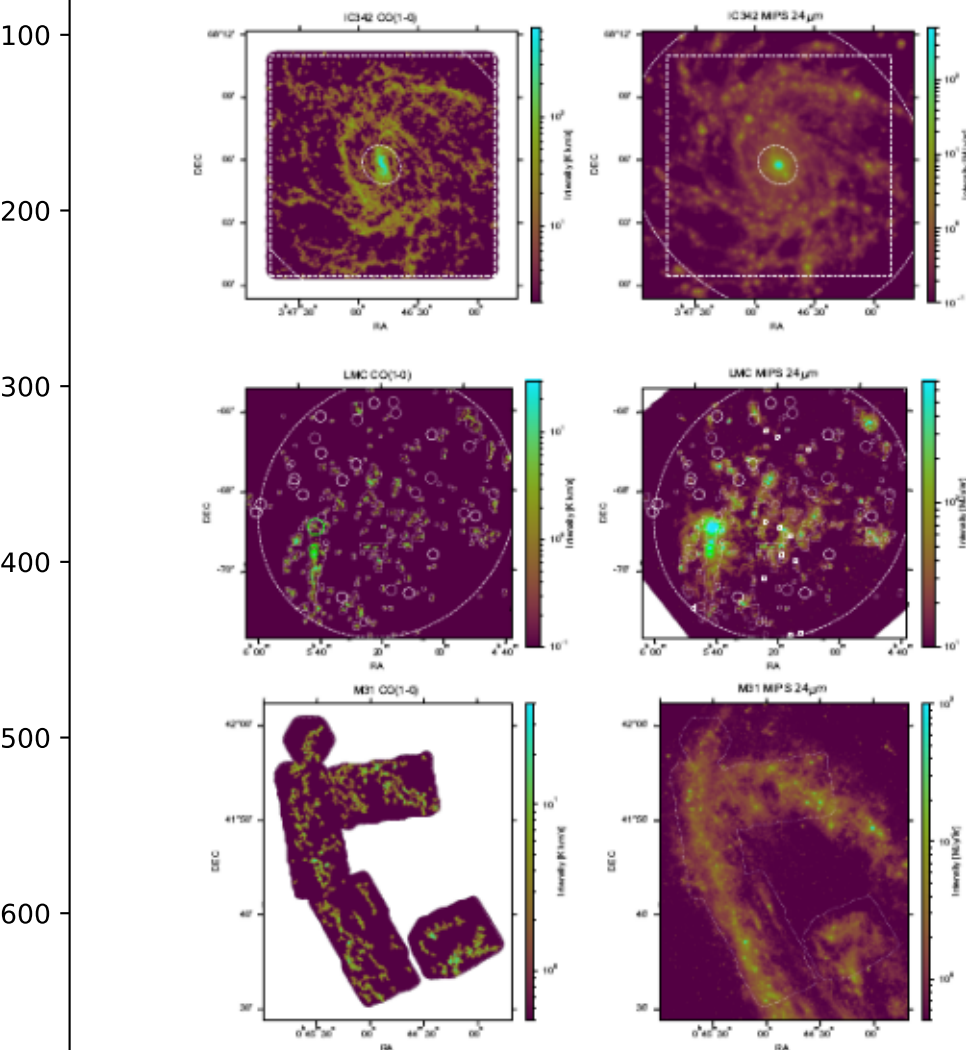
7 Data underlying this article will be shared on reasonable request to the corresponding author.

REFERENCES

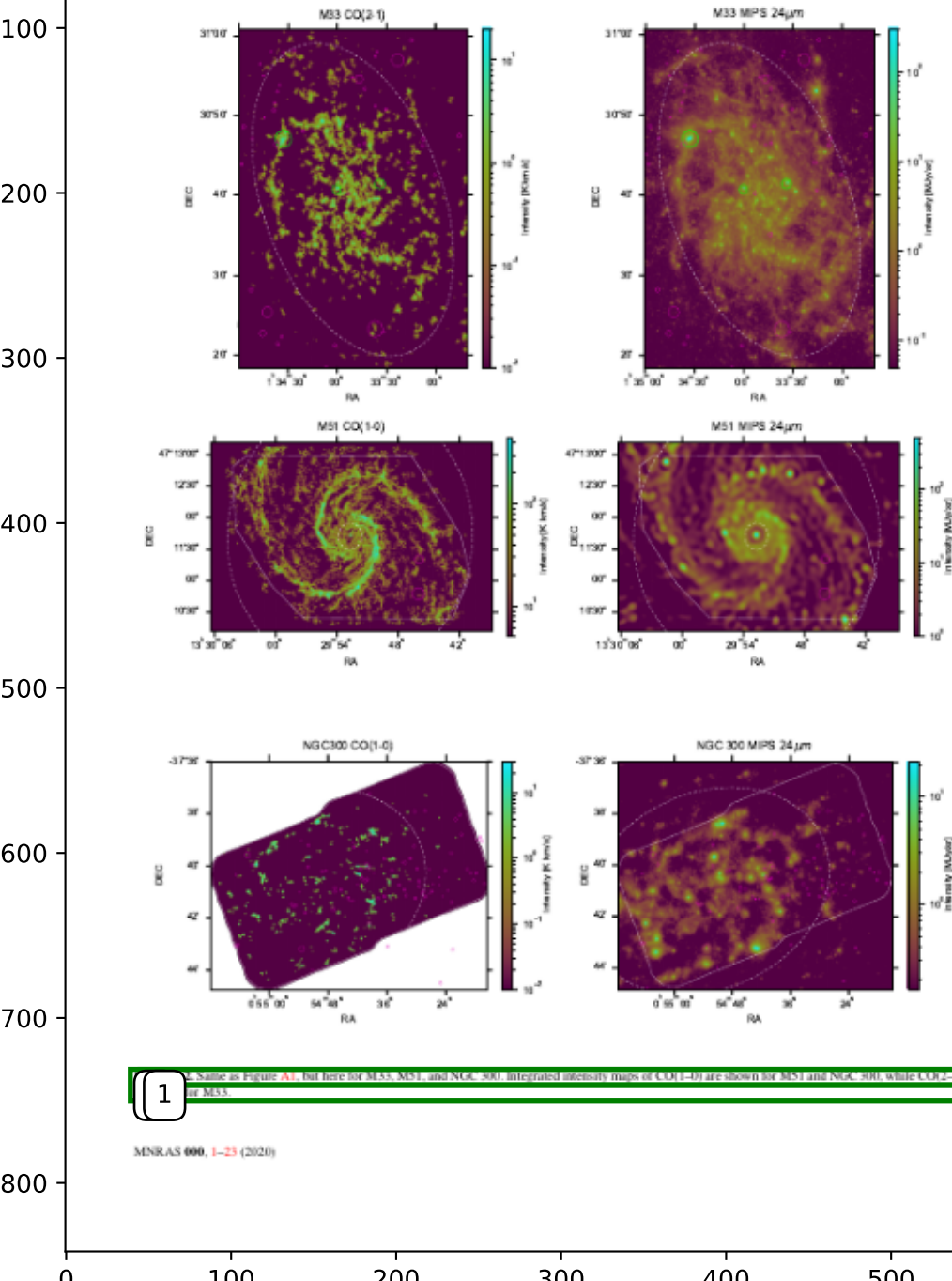
8 (et al. 2020, *Nature*, 578, 287); Draine B. T., Gordon K. D., Sandstrom K., 2011, *PASP*, 123,

- 2 [Carrasco N., Santos J. J., Scott P., 2008, *MNRAS*, **387**, 845–854](#)
 3 [Marciniak R., Barnby F., 2011, *AJ*, **142**, 139](#)
 4 [Verasamy T., Thomson T., Abdalla J., 2005, *Hiro: Simulation for the Spitzer Space Telescope*, p. 61](#)
 5 [Baines A. T., Longmore S. N., Dale J. E., Krumholz M. R., Krajcik J. M. D., Bigiel F., 2020, *MNRAS*, **498**, 4906](#)
 6 [Bigiel F., Leroy A., Walter F., Brinks E., de Blok W. J. G., Madore B., Thornley M. D., 2008, *AJ*, **136**, 2846](#)
 7 [Blitz L., Fukui Y., Kawamura A., Leroy A., Mizuno N., Rosolowsky E., 2007, in: Reipurth B., Jewitt D., Keil K., eds. *Protostars and Planets V*, p. 81 \[\[arXiv:astro-ph/0602269\]\(#\)\]](#)
 8 [van der Marel R. P., Vacca W. D., 1999, *AJ*, **118**, 831](#)
 9 [A. D., Wolfire M., Leroy A. K., 2013, *ARA&A*, **51**, 207](#)
 10 [F., 2011, *ApJ*, **730**, 129](#)
 11 [Caldeira-Prieto A., Schruba A., 2016, *AJ*, **151**, 34](#)
 12 [Calzetti D., et al., 2005, *ApJ*, **633**, 871](#)
 13 [Calzetti D., et al., 2007, *ApJ*, **666**, 870](#)
 14 [Calzetti D., et al., 2015, *ApJ*, **811**, 75](#)
 15 [Cardelli J. A., Clayton G. C., Mathis J. S., 1989, *ApJ*, **345**, 245](#)
 16 [Chevance M., et al., 2020a, arXiv e-prints, p. \[arXiv:2010.13788\]\(#\)](#)
 17 [Chevance M., et al., 2020b, *space*, **68**, 100, 1–10](#)
 18 [Chevance M., et al., 2020c, *MNRAS*, **493**, 2872](#)
 19 [Colombo D., et al., 2014, *ApJ*, **784**, 4](#)
 20 [Cox T. J., et al., 2011, *ApJ*, **731**, 109](#)
 21 [Cox T. J., et al., 2017, *AA*, **601**, A146](#)
 22 [Dakamani J. J., et al., 2009, *ApJS*, **183**, 67](#)
 23 [Dakamani J. J., et al., 2012, *ApJS*, **200**, 18](#)
 24 [Dale J. E., 2015, *New Astron. Rev.*, **68**, 1](#)
 25 [Dale D. A., et al., 2007, *ApJ*, **655**, 863](#)
 26 [Dale D. A., et al., 2009, *ApJ*, **703**, 517](#)
 27 [Draine B. T., Li A., 2007, *ApJ*, **657**, 810](#)
 28 [Draine B. T., et al., 2007, *ApJ*, **663**, 866](#)
 29 [Draine C., et al., 2014, *AA*, **567**, A118](#)
 30 [Dumas G., Schinnerer E., Tabatabaei F. S., Beck R., Verasamy T., Murphy C., 2014, *ApJ*, **787**, 124](#)
 31 [Elmegreen B. G., 1998, *MNRAS*, **299**, 588](#)
 32 [Elmegreen B. G., 2000, *ApJ*, **530**, 277](#)
 33 [Elmegreen B. G., Elmegreen D. M., 2019, *ApJS*, **245**, 14](#)
 34 [Elmegreen B. G., Elmegreen D. M., 2020, *ApJ*, **95**, 71](#)
 35 [Enriquez G., Plumbe R. I., Rosolowsky E., Blitz L., 2003, *ApJS*, **149**, 343](#)
 36 [F. I., et al., 2007, *ApJS*, **171**, 16](#)
 37 [F. I., Lada C. J., Forbrich J., Mentes K. M., Bouy H., 2014, *ApJ*, **814**, 16](#)
 38 [F. I., Lada E. A., 2003, *AA*, **401**, 105](#)
 39 [F. I., Gnedin N. Y., Kravtsov A. V., 2011, *ApJ*, **732**, 115](#)
 40 [F. I., Lada E. A., 2003, *PASP*, **115**, 63](#)
 41 [F. I., Lada E. A., 1999, *PASP*, **111**, 320](#)
 42 [F. I., Lada E. A., 2007, *ApJ*, **663**, 320](#)
 43 [Font G. P., et al., 2013, *ApJ*, **769**, 55](#)
 44 [Fukui Y., et al., 2008, *ApJS*, **178**, 56](#)
 45 [Gaia Collaboration, et al., 2018, *AA*, **616**, A1](#)
 46 [Gamstad J. E., McCullough P. R., Rosing W., Van Buren D., 2001, *PASP*, **113**, 1003](#)
 47 [Gardiner J. K., et al., 2013, *ApJ*, **773**, 69](#)
 48 [Gardiner J. K. D., et al., 2006, *ApJ*, **638**, L87](#)
 49 [Gardiner J. K. D., et al., 2018, *MNRAS*, **481**, 1016](#)
 50 [Grasha K., et al., 2019, *MNRAS*, **483**, 4307](#)
 51 [Gratier P., et al., 2010, *AA*, **522**, A3](#)
 52 [Greenaway B. E., 1998, PhD thesis, NEW MEXICO STATE UNIVERSITY](#)
 53 [Gutierrez D., 2009, *ApJ*, **138**, 1241](#)
 54 [H. L., 2001, *AJ*, **121**, 1030](#)
 55 [Longmore S. N., 2020a, *MNRAS*, **497**, 5076](#)
 56 [Longmore S. N., Krajcik J. M. D., Chevance M., Hygate A. P. S., Krumholz M. R., Schruba A., Langmore S. N., 2020b, *MNRAS*, **498**, 235](#)
 57 [Henshaw J. D., et al., 2020, *Nature Astronomy*, **4**, 1064](#)
 58 [Herrera C. N., et al., 2020, arXiv e-prints, p. \[arXiv:2009.07280\]\(#\)](#)
 59 [Kang X., Chang R., Yin J., Hou J., Zhang F., Zhang Y., Han Z., 2012, *arXiv e-prints*, \[arXiv:1204.0403\]\(#\)](#)
 60 [Kang F., Chang R., Wang L., Cheng L., 2016, *AA*, **585**, A33](#)
 61 [Kang F., Chang R., Wang L., Cheng L., 2016, *AA*, **585**, A33](#)
 62 [Kang F., Chang R., Wang L., Cheng L., 2016, *AA*, **585**, A33](#)
 63 [Kang F., Chang R., Wang L., Cheng L., 2016, *AA*, **585**, A33](#)
 64 [Kang F., Chang R., Wang L., Cheng L., 2016, *AA*, **585**, A33](#)
 65 [Kang F., Chang R., Wang L., Cheng L., 2016, *AA*, **585**, A33](#)
 66 [Kang F., Chang R., Wang L., Cheng L., 2016, *AA*, **585**, A33](#)
 67 [Kang F., Chang R., Wang L., Cheng L., 2016, *AA*, **585**, A33](#)
 68 [Kang F., Chang R., Wang L., Cheng L., 2016, *AA*, **585**, A33](#)
 69 [Kang F., Chang R., Wang L., Cheng L., 2016, *AA*, **585**, A33](#)
 70 [Kang F., Chang R., Wang L., Cheng L., 2016, *AA*, **585**, A33](#)
 71 [Kang F., Chang R., Wang L., Cheng L., 2016, *AA*, **585**, A33](#)
 72 [Kang F., Chang R., Wang L., Cheng L., 2016, *AA*, **585**, A33](#)
 73 [Kang F., Chang R., Wang L., Cheng L., 2016, *AA*, **585**, A33](#)
 74 [Kang F., Chang R., Wang L., Cheng L., 2016, *AA*, **585**, A33](#)
 75 [Kang F., Chang R., Wang L., Cheng L., 2016, *AA*, **585**, A33](#)
 76 [Kang F., Chang R., Wang L., Cheng L., 2016, *AA*, **585**, A33](#)
 77 [Kang F., Chang R., Wang L., Cheng L., 2016, *AA*, **585**, A33](#)
 78 [Kang F., Chang R., Wang L., Cheng L., 2016, *AA*, **585**, A33](#)
 79 [Kang F., Chang R., Wang L., Cheng L., 2016, *AA*, **585**, A33](#)
 80 [Kang F., Chang R., Wang L., Cheng L., 2016, *AA*, **585**, A33](#)
 81 [Kang F., Chang R., Wang L., Cheng L., 2016, *AA*, **585**, A33](#)
 82 [Kang F., Chang R., Wang L., Cheng L., 2016, *AA*, **585**, A33](#)
 83 [Kang F., Chang R., Wang L., Cheng L., 2016, *AA*, **585**, A33](#)
 84 [Kang F., Chang R., Wang L., Cheng L., 2016, *AA*, **585**, A33](#)
 85 [Kang F., Chang R., Wang L., Cheng L., 2016, *AA*, **585**, A33](#)
 86 [Kang F., Chang R., Wang L., Cheng L., 2016, *AA*, **585**, A33](#)
 87 [Kang F., Chang R., Wang L., Cheng L., 2016, *AA*, **585**, A33](#)
 88 [Kang F., Chang R., Wang L., Cheng L., 2016, *AA*, **585**, A33](#)
 89 [Kang F., Chang R., Wang L., Cheng L., 2016, *AA*, **585**, A33](#)
 90 [Kang F., Chang R., Wang L., Cheng L., 2016, *AA*, **585**, A33](#)
 91 [Kang F., Chang R., Wang L., Cheng L., 2016, *AA*, **585**, A33](#)
 92 [Kang F., Chang R., Wang L., Cheng L., 2016, *AA*, **585**, A33](#)
 93 [Kang F., Chang R., Wang L., Cheng L., 2016, *AA*, **585**, A33](#)
 94 [Kang F., Chang R., Wang L., Cheng L., 2016, *AA*, **585**, A33](#)
 95 [Kang F., Chang R., Wang L., Cheng L., 2016, *AA*, **585**, A33](#)
 96 [Kang F., Chang R., Wang L., Cheng L., 2016, *AA*, **585**, A33](#)
 97 [Kang F., Chang R., Wang L., Cheng L., 2016, *AA*, **585**, A33](#)
 98 [Kang F., Chang R., Wang L., Cheng L., 2016, *AA*, **585**, A33](#)
 99 [Kang F., Chang R., Wang L., Cheng L., 2016, *AA*, **585**, A33](#)
 100 [Kang F., Chang R., Wang L., Cheng L., 2016, *AA*, **585**, A33](#)
 101 [Kang F., Chang R., Wang L., Cheng L., 2016, *AA*, **585**, A33](#)
 102 [Kang F., Chang R., Wang L., Cheng L., 2016, *AA*, **585**, A33](#)
 103 [Kang F., Chang R., Wang L., Cheng L., 2016, *AA*, **585**, A33](#)
 104 [Kang F., Chang R., Wang L., Cheng L., 2016, *AA*, **585**, A33](#)
 105 [Kang F., Chang R., Wang L., Cheng L., 2016, *AA*, **585**, A33](#)
 106 [Kang F., Chang R., Wang L., Cheng L., 2016, *AA*, **585**, A33](#)
 107 [Kang F., Chang R., Wang L., Cheng L., 2016, *AA*, **585**, A33](#)
 108 [Kang F., Chang R., Wang L., Cheng L., 2016, *AA*, **585**, A33](#)
 109 [Kang F., Chang R., Wang L., Cheng L., 2016, *AA*, **585**, A33](#)
 110 [Kang F., Chang R., Wang L., Cheng L., 2016, *AA*, **585**, A33](#)
 111 [Kang F., Chang R., Wang L., Cheng L., 2016, *AA*, **585**, A33](#)
 112 [Kang F., Chang R., Wang L., Cheng L., 2016, *AA*, **585**, A33](#)
 113 [Kang F., Chang R., Wang L., Cheng L., 2016, *AA*, **585**, A33](#)
 114 [Kang F., Chang R., Wang L., Cheng L., 2016, *AA*, **585**, A33](#)
 115 [Kang F., Chang R., Wang L., Cheng L., 2016, *AA*, **585**, A33](#)
 116 [Kang F., Chang R., Wang L., Cheng L., 2016, *AA*, **585**, A33](#)
 117 [Kang F., Chang R., Wang L., Cheng L., 2016, *AA*, **585**, A33](#)
 118 [Kang F., Chang R., Wang L., Cheng L., 2016, *AA*, **585**, A33](#)
 119 [Kang F., Chang R., Wang L., Cheng L., 2016, *AA*, **585**, A33](#)
 120 [Kang F., Chang R., Wang L., Cheng L., 2016, *AA*, **585**, A33](#)
 121 [Kang F., Chang R., Wang L., Cheng L., 2016, *AA*, **585**, A33](#)
 122 [Kang F., Chang R., Wang L., Cheng L., 2016, *AA*, **585**, A33](#)
 123 [Kang F., Chang R., Wang L., Cheng L., 2016, *AA*, **585**, A33](#)
 124 [Kang F., Chang R., Wang L., Cheng L., 2016, *AA*, **585**, A33](#)
 125 [Kang F., Chang R., Wang L., Cheng L., 2016, *AA*, **585**, A33](#)
 126 [Kang F., Chang R., Wang L., Cheng L., 2016, *AA*, **585**, A33](#)
 127 [Kang F., Chang R., Wang L., Cheng L., 2016, *AA*, **585**, A33](#)
 128 [Kang F., Chang R., Wang L., Cheng L., 2016, *AA*, **585**, A33](#)
 129 [Kang F., Chang R., Wang L., Cheng L., 2016, *AA*, **585**, A33](#)
 130 [Kang F., Chang R., Wang L., Cheng L., 2016, *AA*, **585**, A33](#)
 131 [Kang F., Chang R., Wang L., Cheng L., 2016, *AA*, **585**, A33](#)
 132 [Kang F., Chang R., Wang L., Cheng L., 2016, *AA*, **585**, A33](#)
 133 [Kang F., Chang R., Wang L., Cheng L., 2016, *AA*, **585**, A33](#)
 134 [Kang F., Chang R., Wang L., Cheng L., 2016, *AA*, **585**, A33](#)
 135 [Kang F., Chang R., Wang L., Cheng L., 2016, *AA*, **585**, A33](#)
 136 [Kang F., Chang R., Wang L., Cheng L., 2016, *AA*, **585**, A33](#)
 137 [Kang F., Chang R., Wang L., Cheng L., 2016, *AA*, **585**, A33](#)
 138 [Kang F., Chang R., Wang L., Cheng L., 2016, *AA*, **585**, A33](#)
 139 [Kang F., Chang R., Wang L., Cheng L., 2016, *AA*, **585**, A33](#)
 140 [Kang F., Chang R., Wang L., Cheng L., 2016, *AA*, **585**, A33](#)
 141 [Kang F., Chang R., Wang L., Cheng L., 2016, *AA*, **585**, A33](#)
 142 [Kang F., Chang R., Wang L., Cheng L., 2016, *AA*, **585**, A33](#)
 143 [Kang F., Chang R., Wang L., Cheng L., 2016, *AA*, **585**, A33](#)
 144 [Kang F., Chang R., Wang L., Cheng L., 2016, *AA*, **585**, A33](#)
 145 [Kang F., Chang R., Wang L., Cheng L., 2016, *AA*, **585**, A33](#)
 146 [Kang F., Chang R., Wang L., Cheng L., 2016, *AA*, **585**, A33](#)
 147 [Kang F., Chang R., Wang L., Cheng L., 2016, *AA*, **585**, A33](#)
 148 [Kang F., Chang R., Wang L., Cheng L., 2016, *AA*, **585**, A33](#)
 149 [Kang F., Chang R., Wang L., Cheng L., 2016, *AA*, **585**, A33](#)
 150 [Kang F., Chang R., Wang L., Cheng L., 2016, *AA*, **585**, A33](#)
 151 [Kang F., Chang R., Wang L., Cheng L., 2016, *AA*, **585**, A33](#)
 152 [Kang F., Chang R., Wang L., Cheng L., 2016, *AA*, **585**, A33](#)
 153 [Kang F., Chang R., Wang L., Cheng L., 2016, *AA*, **585**, A33](#)
 154 [Kang F., Chang R., Wang L., Cheng L., 2016, *AA*, **585**, A33](#)
 155 [Kang F., Chang R., Wang L., Cheng L., 2016, *AA*, **585**, A33](#)
 156 [Kang F., Chang R., Wang L., Cheng L., 2016, *AA*, **585**, A33](#)
 157 [Kang F., Chang R., Wang L., Cheng L., 2016, *AA*, **585**, A33](#)
 158 [Kang F., Chang R., Wang L., Cheng L., 2016, *AA*, **585**, A33](#)
 159 [Kang F., Chang R., Wang L., Cheng L., 2016, *AA*, **585**, A33](#)
 160 [Kang F., Chang R., Wang L., Cheng L., 2016, *AA*, **585**, A33](#)
 161 [Kang F., Chang R., Wang L., Cheng L., 2016, *AA*, **585**, A33](#)
 162 [Kang F., Chang R., Wang L., Cheng L., 2016, *AA*, **585**, A33](#)
 163 [Kang F., Chang R., Wang L., Cheng L., 2016, *AA*, **585**, A33](#)
 164 [Kang F., Chang R., Wang L., Cheng L., 2016, *AA*, **585**, A33](#)
 165 [Kang F., Chang R., Wang L., Cheng L., 2016, *AA*, **585**, A33](#)
 166 [Kang F., Chang R., Wang L., Cheng L., 2016, *AA*, **585**, A33](#)
 167 [Kang F., Chang R., Wang L., Cheng L., 2016, *AA*, **585**, A33](#)
 168 [Kang F., Chang R., Wang L., Cheng L., 2016, *AA*, **585**, A33](#)
 169 [Kang F., Chang R., Wang L., Cheng L., 2016, *AA*, **585**, A33](#)
 170 [Kang F., Chang R., Wang L., Cheng L., 2016, *AA*, **585**, A33](#)
 171 [Kang F., Chang R., Wang L., Cheng L., 2016, *AA*, **585**, A33](#)
 172 [Kang F., Chang R., Wang L., Cheng L., 2016, *AA*, **585**, A33](#)
 173 [Kang F., Chang R., Wang L., Cheng L., 2016, *AA*, **585**, A33](#)
 174 [Kang F., Chang R., Wang L., Cheng L., 2016, *AA*, **585**, A33](#)
 175 [Kang F., Chang R., Wang L., Cheng L., 2016, *AA*, **585**, A33](#)
 176 [Kang F., Chang R., Wang L., Cheng L., 2016, *AA*, **585**, A33](#)
 177 [Kang F., Chang R., Wang L., Cheng L., 2016, *AA*, **585**, A33](#)
 178 [Kang F., Chang R., Wang L., Cheng L., 2016, *AA*, **585**, A33](#)
 179 [Kang F., Chang R., Wang L., Cheng L., 2016, *AA*, **585**, A33](#)
 180 [Kang F., Chang R., Wang L., Cheng L., 2016, *AA*, **585**, A33](#)
 181 [Kang F., Chang R., Wang L., Cheng L., 2016, *AA*, **585**, A33](#)
 182 [Kang F., Chang R., Wang L., Cheng L., 2016, *AA*, **585**, A33](#)
 183 [Kang F., Chang R., Wang L., Cheng L., 2016, *AA*, **585**, A33](#)
 184 [Kang F., Chang R., Wang L., Cheng L., 2016, *AA*, **585**, A33](#)
 185 [Kang F., Chang R., Wang L., Cheng L., 2016, *AA*, **585**, A33](#)
 186 [Kang F., Chang R., Wang L., Cheng L., 2016, *AA*, **585**, A33](#)
 187 [Kang F., Chang R., Wang L., Cheng L., 2016, *AA*, **585**, A33](#)
 188 [Kang F., Chang R., Wang L., Cheng L., 2016, *AA*, **585**, A33](#)
 189 [Kang F., Chang R., Wang L., Cheng L., 2016, *AA*, **585**, A33](#)
 190 [Kang F., Chang R., Wang L., Cheng L., 2016, *AA*, **585**, A33](#)
 191 [Kang F., Chang R., Wang L., Cheng L., 2016, *AA*, **585**, A33](#)
 192 [Kang F., Chang R., Wang L., Cheng L., 2016, *AA*, **585**, A33](#)
 193 [Kang F., Chang R., Wang L., Cheng L., 2016, *AA*, **585**, A33](#)
 194 [Kang F., Chang R., Wang L., Cheng L., 2016, *AA*, **585**, A33](#)
 195 [Kang F., Chang R., Wang L., Cheng L., 2016, *AA*, **585**, A33](#)
 196 [Kang F., Chang R., Wang L., Cheng L., 2016, *AA*, **585**, A33](#)
 197 [Kang F., Chang R., Wang L., Cheng L., 2016, *AA*, **585**, A33](#)
 198 [Kang F., Chang R., Wang L., Cheng L., 2016, *AA*, **585**, A33](#)
 199 [Kang F., Chang R., Wang L., Cheng L., 2016, *AA*, **585**, A33](#)
 200 [Kang F., Chang R., Wang L., Cheng L., 2016, *AA*, **585**, A33](#)
 201 [Kang F., Chang R., Wang L., Cheng L., 2016, *AA*, **585**, A33](#)
 202 [Kang F., Chang R., Wang L., Cheng L., 2016, *AA*, **585**, A33](#)
 203 [Kang F., Chang R., Wang L., Cheng L., 2016, *AA*, **585**, A33](#)
 204 [Kang F., Chang R., Wang L., Cheng L., 2016, *AA*, **585**, A33](#)
 205 [Kang F., Chang R., Wang L., Cheng L., 2016, *AA*, **585**, A33](#)
 206 [Kang F., Chang R., Wang L., Cheng L., 2016, *AA*, **585**, A33](#)
 207 [Kang F., Chang R., Wang L., Cheng L., 2016, *AA*, **585**, A33](#)
 208 [Kang F., Chang R., Wang L., Cheng L., 2016, *AA*, **585**, A33](#)
 209 [Kang F., Chang R., Wang L., Cheng L., 2016, *AA*, **585**, A33](#)
 210 [Kang F., Chang R., Wang L., Cheng L., 2016, *AA*, **585**, A33](#)
 211 [Kang F., Chang R., Wang L., Cheng L., 2016, *AA*, **585**, A33](#)
 212 [Kang F., Chang R., Wang L., Cheng L., 2016, *AA*, **585**, A33](#)
 213 [Kang F., Chang R., Wang L., Cheng L., 2016, *AA*, **585**, A33](#)
 214 [Kang F., Chang R., Wang L., Cheng L., 2016, *AA*, **585**, A33](#)
 215 [Kang F., Chang R., Wang L., Cheng L., 2016, *AA*, **585**, A33](#)
 216 [Kang F., Chang R., Wang L., Cheng L., 2016, *AA*, **585**, A33](#)
 217 [Kang F., Chang R., Wang L., Cheng L., 2016, *AA*, **585**, A33](#)
 218 [Kang F., Chang R., Wang L., Cheng L., 2016, *AA*, **585**, A33](#)
 219 [Kang F., Chang R., Wang L., Cheng L., 2016, *AA*, **585**, A33](#)
 220 [Kang F., Chang R., Wang L., Cheng L., 2016, *AA*, **585**, A33](#)
 221 [Kang F., Chang R., Wang L., Cheng L., 2016, *AA*, **585**, A33](#)
 222 [Kang F., Chang R., Wang L., Cheng L., 2016, *AA*, **585**, A33](#)
 223 [Kang F., Chang R., Wang L., Cheng L., 2016, *AA*, **585**, A33](#)
 224 [Kang F., Chang R., Wang L., Cheng L., 2016, *AA*, **585**, A33](#)
 225 [Kang F., Chang R., Wang L., Cheng L., 2016, *AA*, **585**, A33](#)
 226 [Kang F., Chang R., Wang L., Cheng L., 2016, *AA*, **585**, A33](#)
 227 [Kang F., Chang R., Wang L., Cheng L., 2016, *AA*, **585**, A33](#)
 228 [Kang F., Chang R., Wang L., Cheng L., 2016, *AA*, **585**, A33](#)
 229 [Kang F., Chang R., Wang L., Cheng L., 2016, *AA*, **585**, A33](#)
 230 [Kang F., Chang R., Wang L., Cheng L., 2016, *AA*, **585**, A33](#)
 231 [Kang F., Chang R., Wang L., Cheng L., 2016, *AA*, **585**, A33](#)
 232 [Kang F., Chang R., Wang L., Cheng L., 2016, *AA*, **585**, A33](#)
 233 [Kang F., Chang R., Wang L., Cheng L., 2016, *AA*, **585**, A33](#)
 234 [Kang F., Chang R., Wang L., Cheng L., 2016, *AA*, **585**, A33](#)
 235 [Kang F., Chang R., Wang L., Cheng L., 2016, *AA*, **585**, A33](#)
 236 [Kang F., Chang R., Wang L., Cheng L., 2016, *AA*, **585**, A33](#)
 237 [Kang F., Chang R., Wang L., Cheng L., 2016, *AA*, **585**, A33](#)
 238 [Kang F., Chang R., Wang L., Cheng L., 2016,](#)





0 L Maps of CO(1-0) emission (left panels) and 24 μ m emission (right panels) for the IC 342, LMC, and M31. The ranges of galactic radii included in the maps are indicated by white dashed ellipses. The white dotted line shows the coverage of the CO observations. In the LMC, regions where molecular clouds were observed but was not targeted by the MAGMA survey are masked (white solid circles). The masked bright star-forming regions are shown by green circles. We also mask foreground stars, background galaxies, and map artifacts (purple circles)



1
Same as Figure A1, but here for M33, M51, and NGC 300. Integrated intensity maps of CO(1-0) are shown for M51 and NGC 300, while CO(2-1) for M33.

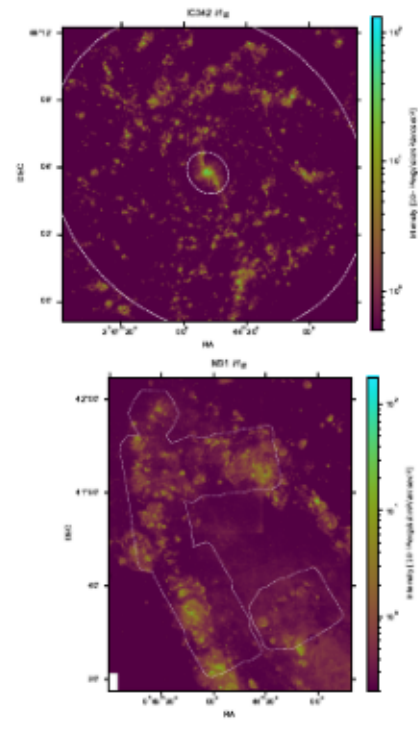


Fig. B1. Same as Figure A2, for H α emission maps of IC 342 and M33.

ments such as M31 ($\sim 1 M_{\odot} pc^{-3}$). The duration over which H α emission overlap is short ($2.2^{+0.4}_{-0.5}$ Myr in IC 342 and $1.5^{+0.3}_{-0.4}$ Myr in M31), as seen in previous measurements of other galaxies (Chevance et al. 2020a). These short feedback timescales indicate that molecular clouds are destroyed shortly after the star-forming region becomes exposed, making them visible in H α . Finally, we find that independent star-forming regions are separated by 120^{+10}_{-10} pc in IC 342 and 181^{+28}_{-19} pc in M31, comparable to our measurements with 24 μm as an SFR tracer, as well as our previous findings with H α for different galaxies.

3 Universität Heidelberg, Mönchhofstraße 12-14, 69120 Heidelberg

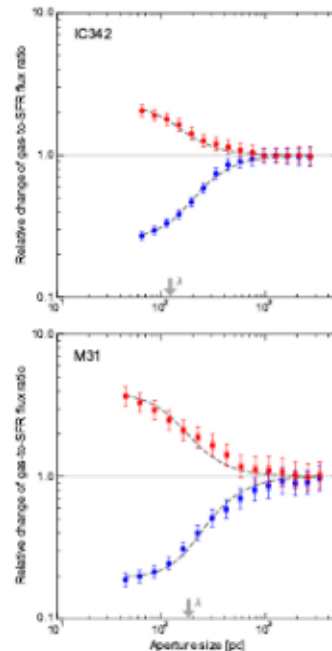
Max-Planck-Institut für Extraterrestrische Physik, Giessenbachstraße 1, 85748 Garching, Germany

¹Center for Astrophysics and Space Sciences, Department of Physics, University of California, San Diego, 9500 Gilman Drive, La Jolla, CA 92093, USA

⁴Amplander Institut für Astronomie, Universität Bayreuth, Auf der Morgenstelle 10, D-9544 Bayreuth, Germany

4 4. Mass input parameters of the analysis using *Bir* as an SFR tracer
2 and *M31*. For other input parameters, we use the default values
table 2 of *Krijssen et al.* (2018).

Quantity	IC 342	M31
$t_{\text{quench}} [\text{pc}]$	65	45
$t_{\text{quench}} [\text{pc}]$	3000	4000
N_{H}	15	15
$N_{\text{H, min}}$	10	20
$\Delta \log \langle T \rangle_{\text{CO}}$	1.1	1.2
$\Delta \log \langle T \rangle_{\text{CD}}$	0.05	0.05
$\Delta \log \langle T \rangle_{\text{IR}}$	2.8	2.0
$\Delta \log \langle T \rangle_{\text{He}}$	0.05	0.1
$t_{\text{ff}} [\text{Myr}]$	4.25	4.42
$t_{\text{infall, inf}} [\text{Myr}]$	0.15	0.18
$t_{\text{infall, inf}} [\text{Myr}]$	0.15	0.19
n_{H}	12	10



5 12. Relative change in the gas-to-H₂ (C₂₀-H₂) flux ratio compared to the galactic average as a function of size of apertures placed around the H₂ (red) emission peaks. The error bars indicate 1 σ uncertainty on each individual data point whereas the shaded area is an effective 1 σ uncertainty taking into account the covariance between data points. Our best-fitting model is shown as dashed line and the solid horizontal line indicates the galactic average. The measured region separation length (λ) is indicated in each panel and other constrained best-fitting parameters (θ_{ex} and $r_{\text{in}, \text{H}_2}$) are listed in Table 3.

1

Deutsches Zentrum für Luft- und Raumfahrt e.V., Germany
Observatories of the Carnegie Institution for Science, 813
Marshall Street, Pasadena, CA 91101, USA

¹*Departamento de Astronomía, Universidad de Chile, Casilla*
36-D, Santiago, Chile

²*Aix Marseille Univ, CNRS, CNES, LAM (Laboratoire*
d'Astrophysique de Marseille), Marseille, France

³*Department of Physics & Astronomy, University of Wyoming,*
Laramie, WY 82071

⁴*Department of Astronomy, University of Massachusetts - Amherst,*
710 N. Pleasant St., Amherst, MA 01003

¹⁰*Institut für Theoretische Astrophysik, Zentrum für Astronomie*
der Universität Heidelberg, Albert-Ueberle-Strasse 2, 69120
Heidelberg, Germany

2

Open School of Astronomy and Astrophysics, Australian
Capital University, Canberra, ACT 2611, Australia

⁵*National Centre for Radio Astronomy Research, University*
of Western Australia, 7 Fairway, Crawley, 6009, WA, Australia

¹¹*IRAM, 300 rue de la Picardie, 38406 Saint Martin d'Hères,*
France

¹⁴*Universität Heidelberg, Interdisziplinäres Zentrum für Wis-*
senschaftlicher Rechnen im Neuenheimer Feld 265, 69120

3

Heidelberg, Germany
300 IPAC MC 314-6 (Keith Spalding Building) 1200 E
Montgomery Blvd Pasadena, CA 91125

¹⁶*Department of Astronomy, The Ohio State University, 140 West*
18th Ave, Columbus, OH 43210, USA

¹⁷*Sorbonne Université, Observatoire de Paris, Université PSL,*
CNRS, LERMA, F-75005, Paris, France

¹⁸*Observatorio Astronómico Nacional (IGN), C/Alfonso XII 3,*
Madrid E-28014, Spain

¹⁹*Max-Planck-Institut für Astronomie, Königstuhl 17, 69117*
Heidelberg, Germany

4

This paper has been typeset from a L^aT_EX/L^aT_EX file prepared by the author